Nonintrusive Diagnostic Strategies for Arcjet Stream Characterization

Presented by
Douglas G. Fletcher
Reacting Flow Environments Branch, MS 230-2
NASA Ames Research Center
Moffett Field, CA, 94035-1000

Paper presented at the RTO AVT Course on "Measurement Techniques for High Enthalpy and Plasma Flows", held in Rhode-Saint-Genèse, Belgium, 25-29 October 1999, and published in RTO EN-8.

1. Introduction

In the previous lecture, the issues related to arcjet flow modeling were introduced, and the limitations of conventional instrumentation in addressing these issues were discussed. The general level of understanding of the arcjet flows was seen to preclude the use of arcjets as aerothermodynamic test facilities beyond the current role in aerothermal material testing, despite their long test duration capability. In this section, the focus will be on new developments in spectroscopic instrumentation and techniques that can be brought to bear on the fundamental problem of arcjet stream characterization. Although a wide selection of arcjet facilities were introduced in the previous section, the discussion of nonintrusive diagnostic instrumentation will be restricted to the large-scale, segmented, constricted-arc heater facilities that are most widely used in thermal protection material testing for aerospace applications.

After a brief review of the important features of arcjet flows, the topic of nonintrusive, optical diagnostics is introduced with a discussion of some of the basic aspects of radiative transitions. The lecture is then organized into two sections covering emission measurements and laser-induced fluorescence measurements. Emission measurements are presented next for different regions of arcjet flows, while the fluorescence measurements are presented for the free stream region only. Summaries are given for each of the two main sections, and observations on arcjet characterization by optical diagnostics in general are given at the end.

Characterization of arcjet flows involves determining the thermodynamic state of the test gas. To do this in any particular flow region requires an evaluation of the distribution of energy among the kinetic, chemical, and thermal modes of the gas, which also quantifies the degree of departure from thermochemical equilibrium. As opposed to other high enthalpy ground-test facilities, the total enthalpy of an arcjet flow is not always known, so characterization will also involve determining the total enthalpy. Although the measurement objectives can be clearly and simply stated, the nonequilibrium nature of typical arcjet flows makes arcjet characterization difficult to accomplish by requiring measurements of multiple species and multiple temperatures in addition to the flow velocity.

1.1 Ames AHF Arcjet Facility

The Aerodynamic Heating Facility (AHF) Arcjet at NASA Ames Research Center is one example of a large-scale, constricted-arc heater test facility. It consists of a segmented, constricted-arc heater, a conical nozzle section, and a test cabin.[1] The arrangement of these components is shown in Fig. 1. Facility operation is initiated by evacuating the arcjet facility and then striking an arc in a low-pressure argon stream. The test gas flow, which typically consists of air or nitrogen, is then added and the arc current is adjusted to achieve the desired test conditions. Within the arc heater, the incoming test gas flow is heated by the electrical discharge to a level that causes substantial dissociation of the molecular species. The argon stream used to initiate the arc is maintained during operation and an additional argon stream is injected in the downstream electrode package to minimize erosion. This electrode package also serves as a plenum that reduces the gas velocity before it enters the nozzle. The flow is then accelerated to high velocity through a conical, converging-diverging nozzle. Owing to the decrease in density during the expansion, the collision frequency decreases rapidly in the nozzle and the thermochemical state of the flow departs from equilibrium. At some point in the nozzle, depending on the test conditions, the flow chemistry becomes frozen, and remains frozen through the remainder of the expansion. Various nozzle sections can be used to provide expansion ratios ranging from 64 to 576. The flow exits the nozzle and continues expanding into a cabin where material tests are conducted. Material samples are typically inserted into the stream ≈36 cm downstream of the nozzle exit.

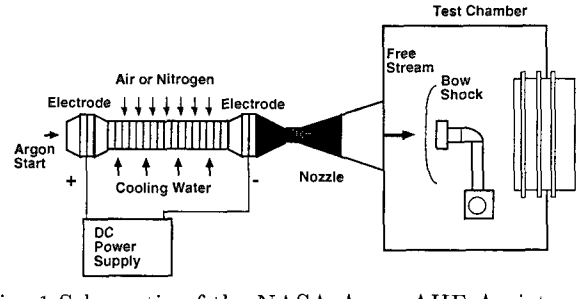

Fig. 1 Schematic of the NASA Ames AHF Arcjet.

The constrictor chamber pressure and arc current are adjusted to achieve the desired operating condition, which is usually defined by a predetermined surface temperature or heat flux level impinging on the test article. Test durations of up to 20 minutes are possible, depending on the particular conditions. During the tests, the stagnation pressure, cabin pressure, and arc heater conditions are continuously monitored. Stagnation-point heating and pitot pressure measurements are typically performed during a run to verify test conditions. These measurements are also frequently used to determine the stream enthalpy based on an empirical correlation for stagnation point heating. The limitations of this approach for characterizing the arcjet stream were discussed in the previous lecture.

The general state of arcjet stream characterization in the early 90's was summarized in an excellent and thorough review article by Scott.[2] Both conventional instrumentation and nonintrusive, spectroscopic techniques that were being developed for arcjet flow characterization were critically reviewed in the article.

Particular attention was given to how various diagnostic techniques could be used to characterize the most important stream variables: enthalpy and the degree of nonequilibrium. Instead of revisiting all of the instrumental approaches that have been used for making measurements in arcjet flows, this lecture will focus on recent developments in nonintrusive optical techniques that have been implemented in large-scale arcjet facilities. Progress made in arcjet characterization using these optical diagnostics will be discussed in detail.

1.2 Nonintrusive Diagnostics

Stated in the most general terms, optically based, nonintrusive diagnostic strategies attempt to determine flow or thermodynamic properties from an analysis of light that is emitted from either a thermally-induced or laser-induced process. Optical techniques have been used for many years in spectroscopic investigations and aerospace diagnostic applications. Most of the earlier applications involved radiative emission and absorption in addition to interferometric and shadowgraph instrumentation. In fact, early in the development stage of large-scale arcjet facilities, emission spectroscopy was investigated as a means for characterizing a nitrogen shock-layer flow.[3] Newer spectroscopic diagnostic techniques that take advantage of recent advances in laser instrumentation are gaining wider acceptance in the aerospace ground-test community.[4] Much of the development of these instruments, particularly those based on laser spectroscopy, has been driven by research into combustion processes.[5]

Although all of the nonintrusive diagnostic techniques that will be discussed in this paper are derived from the same physical principles, each technique will be examined separately. In addition, mathematical descriptions will be given to illustrate the relation between the measured quantity and the flow variables. To do this adequately requires a brief examination of background material that will be common to all of the techniques. More information on basic principles and on specific diagnostic techniques can be found in books by Eckbreth[5] and Demtröder[6].

Background Physics - Atoms and molecules have discrete, quantized energy levels. For atoms, these energy levels are only electronic, while molecules have rotational and vibrational energy levels in addition to the electronic energy levels. If certain selection criteria, which are established from quantum mechanical considerations,[7] are met, then atoms and molecules can undergo radiative transitions between these levels. These transitions can involve the scattering, absorption, or emission of a photon. Because applications of optical diagnostics to arcjet stream characterization is a major focus of this paper, only processes involving photon emission and absorption will be considered further.

For absorption and emission, the photon energy matches the difference between the two internal (atomic or molecular) states connected by the radiative transition,

$$h\nu = E_u - E_l \quad , \tag{1}$$

where h is the Planck constant and ν is the transition frequency. For atomic species, the energies correspond to electronic levels directly, while for molecules the upper and lower state energies are comprised of electronic, vibrational, and rotational terms,

$$E = T_E + G(v) + F(J) \quad , \tag{2}$$

where v and J are the vibrational and rotational quantum numbers, respectively. For diatomic molecules that are modeled simply as vibrating rotators the vibrational and rotational term energies are represented by polynomial expansions[7] that take into account interactions between these energy modes,

$$G(v) = \omega_e(v+\frac{1}{2}) - \omega_e x_e(v+\frac{1}{2})^2 + \omega_e y_e(v+\frac{1}{2})^3 + ... \tag{3}$$

$$F(J) = [B_e - \alpha_e(v+\frac{1}{2})]J(J+1) - [D_e + \beta_e(v+\frac{1}{2})J^2(J+1)^2 + ... \tag{4}$$

For most species of interest related to arc-heated or shock-heated air, the vibrational and rotational constants $(\omega_e, B_e, D_e, \alpha_e, \beta_e)$ in the above expressions, and in higher order terms, are accurately known. Recommended constants for many diatomic species are given in Huber and Herzberg[8], while Laux[9] has a compilation of more recently reported constants for high temperature air.

The amount of light absorbed or emitted by atoms or molecules in a particular energy level depends on the population in that particular level. If the system is in thermal equilibrium, then the populations of atoms or molecules in the energy levels follow a Boltzmann distribution,[10]

$$N_i = N\frac{g_i e^{(-E_i/kT)}}{\sum_i g_i e^{(-E_i/kT)}} \quad , \tag{5}$$

where g_i is the level degeneracy. The summation in the denominator is over all energy levels, and it is called the partition function, $Q = \sum_i g_i e^{(-E_i/kT)}$. For molecules, the total partition function can be expressed as the product of the partition functions for the individual internal energy modes,

$$Q = Q_R\, Q_V\, Q_E \quad . \tag{6}$$

An approximate closed form expression for the vibrational partition function is

$$Q_V = (1 - e^{-\theta_v/T})^{-1} \quad , \tag{7}$$

where $\theta_v = hc\omega_e/k$ is the characteristic vibrational temperature[10] of the particular molecule under consideration, c is the speed of light, and k is the Boltzmann constant. For room temperature and higher, an approximate closed form expression can also be derived for the rotational partition function,

$$Q_R = \frac{T}{\sigma\theta_r} \quad , \tag{8}$$

where $\theta_r = hcB/k$ is the characteristic rotational temperature of the molecule, and $\sigma = 1$ or 2 depending on whether the diatomic molecule is heteronuclear or homonuclear.

With the aid of these expressions for partition functions, analytic expressions for the fractional populations in particular rotational (J) and vibrational (v) levels can be written as

$$\frac{N_J}{N} = \frac{\sigma(2J+1)\theta_r}{T} e^{-J(J+1)\theta_r/T} \quad , \tag{9}$$

if nuclear spin degeneracy is ignored, and

$$\frac{N_v}{N} = e^{-v\theta_v/T}(1 - e^{-\theta_v/T}) \quad . \tag{10}$$

It should be noted that Eqs. (5), (9), and (10) govern the population distributions of atoms and molecules under thermal equilibrium conditions. By inspection of the exponential terms, it is apparent that the higher energy levels become substantially populated only at very high temperatures.

Uncertainty in Measured Quantities - Both approximate and exact analytical expressions are developed in subsequent sections to relate particular flow properties to either emission or LIF signals. In addition to illustrating how a particular flow property is measured, these expressions provide a means for estimating the sensitivity of the optical signal to that flow property, which is then used to determine the uncertainty. All flow properties determined from optical measurements in this paper include estimates of the experimental uncertainty. These estimates are derived from the combined effect of multiple, statistically independent contributions, which is expressed as

$$\sigma_M = \sqrt{(\frac{\partial M}{\partial W_1}\sigma_{W_1})^2 + (\frac{\partial M}{\partial W_2}\sigma_{W_2})^2 + \ldots.} \quad , \tag{11}$$

where $M = f(W_1, W_2, \ldots)$ and σ represents the uncertainty in a particular parameter. Sensitivity of the measured parameter to a particular variable is reflected in the value of the partial derivative taken with respect to that variable in the above expression.

Some contributions, such as uncertainties in spectroscopic constants, are evaluated analytically, while others, such as unresolved background signal contributions, are evaluated numerically using a spectral model. Detailed discussions of the uncertainty estimates are given in each of the referenced publications that describe a particular experiment. The importance of estimating uncertainties for the measured values cannot be understated, since knowledge of the uncertainty values guides the use of the measurements and informs improvements in instrumentation and diagnostic approach.

2. Emission Measurements in Large-Scale Arcjet Facilities

Emission measurements are the simplest optically based, nonintrusive diagnostics that can be used in arcjet test facilities. These measurements are truly nonintrusive, since only light is taken from the flowfield. No external mechanism is invoked to populate excited atomic or molecular states that would lead to observable radiative transitions. Rather, thermal excitation within the flow region continuously replenishes populations in radiating electronic levels for the constituent atoms and molecules. This excitation mechanism necessarily constrains measurable populations to regions having sufficient thermal excitation, such as shock layers over test articles placed in the stream and regions within and adjacent to the arc heater.

2.1 Emission Spectroscopic Measurements

When the spontaneous emission rate for a particular radiative transition, A_{ul}, is known, then the radiant power density emitted by a unit volume of gas can be expressed as

$$E = n_u A_{ul} h\nu_{ul}/4\pi \quad , \tag{12}$$

where n_u is the number density of the emitting level. The spectral power density of spontaneous emission can be obtained by multiplying the above expression by a line-shape function, $\phi(\lambda)$,

$$E_\lambda = n_u A_{ul} h\nu_{ul}\phi(\lambda)/4\pi \quad , \tag{13}$$

where $\phi(\lambda)$ is defined such that

$$\int_{-\infty}^{+\infty} \phi(\lambda)d\lambda = 1.$$

An optically thin gas, which has negligible self-absorption, is essentially emission dominated. For this special case, stimulated emission is also negligible and the specific intensity (also called spectral radiance) is given by the integral of the spectral power density over

an optical path, which might be defined by a line-of-sight, as

$$I_\lambda = \int_0^L E_\lambda dx \quad .$$

This latter quantity, the specific intensity, is the quantity actually measured by a radiometric sensor (after applying a slit or filter function). Note that the expressions above apply only to atomic and bound-bound molecular radiative transitions. If significant absorption is occurs within the observation volume, then the combined effects of stimulated absorption and emission must be taken into account, and the radiative transport equation takes on a more complex form,[11]

$$I_\lambda = \int_0^L \alpha_\lambda (I_\lambda - B_\lambda) dx \quad ,$$

where α_λ is the effective volumetric absorption coefficient that includes stimulated emission and absorption and B_λ is the Planck function.

For either case, quantitative emission measurements require that the detection system be calibrated with standard spectral lamps. Also, for both cases the intensity measured by the detector is integrated along the optical path and spatial resolution in the line-of-sight direction is therefore lost.

An emission dominated, optically thin gas and an isotropic emitting volume with constant properties represents an optimal diagnostic situation for emission measurements, since the light levels can be interpreted directly in terms of the local thermodynamic properties of the emitting volume. Generally, this is not the case even when the gas is optically thin; usually there are spatial property gradients along the viewing direction and the recorded emission signal represents the intensity-weighted integral sum of the emitted light.[12] For the worst case, which is also quite common, gradients along the line of sight and self-absorption in the optically thick gas require a solution of the radiative transport equation with a numerical model, such as NEQAIR.[13]

For applications of emission spectroscopy to arcjet flow property measurements in large-scale facilities, the test gas is usually a mixture of air and argon (or N_2/argon) and the wavelength range of interest typically covers the region between 2000 and 9000 Å. An example of a measured emission spectrum for this range is shown in Fig. 2a-d. The temperature of the gas was between 7000 and 8000 K, based on an analysis of the spectrally resolved emission. The thermochemical state of the flow was not specified, although it should be close to equilibrium, because the spectrum was acquired in the high pressure region of the arcjet within the downstream electrode package. The emission is a mix of bound electronic transitions from molecules, as evidenced by the band structure at the shorter wavelengths, and from atoms, which appear as isolated lines with increasing intensity at longer wavelengths. There is also an underlying background emission that is at least partly due to bound-free continuum emission, and there may possibly be some black-body emission collected from reflections of the arc in the constrictor region. It will be useful to refer to this spectrum as the relationships between atomic and molecular emission and thermodynamic properties are developed below.

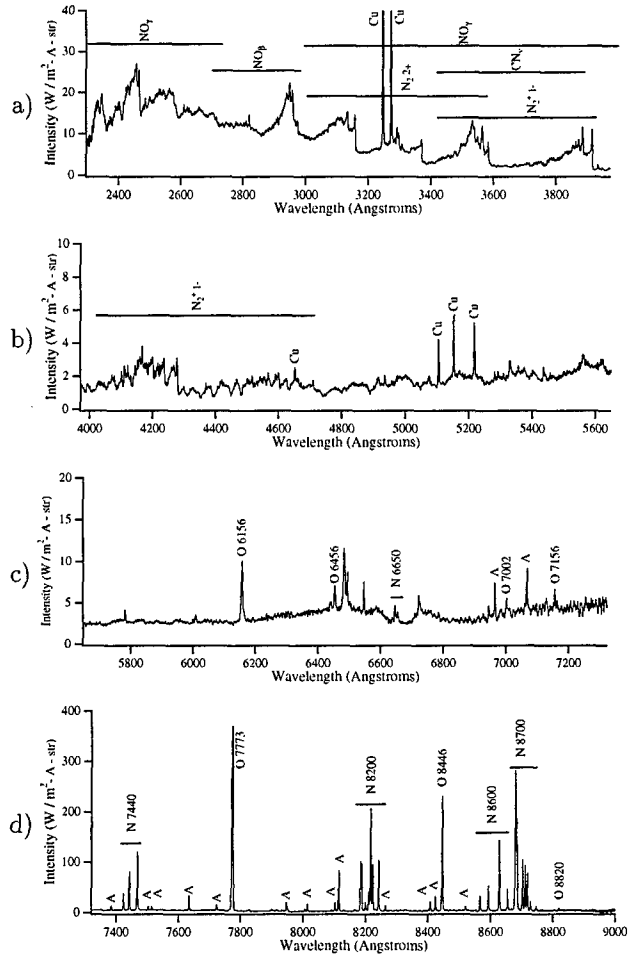

Fig. 2a-d. Spectrally resolved emission from a high temperature mixture of air and argon.

Temperature Measurement - In Eq. (13), the thermodynamic dependence of the emission is due to the upper state population, n_u, which is a function of species density and temperature. Under conditions of thermal equilibrium, the temperature dependence is given by the Boltzmann fraction expression and the specific intensity for emission dominated radiation integrated along the line-of-sight is

$$I_\lambda = \frac{n A_{ul} h\nu_{ul}}{4\pi} \phi(\lambda) \frac{g_u}{Q} e^{-E_u/kT} L \quad . \qquad (14)$$

At modest temperatures, where $E_u/kT > 1$, emission is more sensitive to temperature than to density. The degree of temperature sensitivity is determined by the

energy of the radiating level. If the system is in thermal equilibrium, then in principle, the measurement of two spectral features with different upper state energies is sufficient to determine temperature.

Electronic Temperature - For example, the electronic temperature can be determined from the ratio of the spectrally integrated intensities emanating from two different thermally populated electronic levels of an atomic species. By taking the natural log of the intensity ratio and rearranging the terms, an analytic expression for electronic temperature is obtained,

$$T_e = \frac{(E_1 - E_2)/k}{\ln\left(\frac{I_2 A_1 g_1 \nu_1}{I_1 A_2 g_2 \nu_2}\right)} \quad , \tag{15}$$

where I_1, I_2 are the spectrally integrated intensities,

$$I = \int_{\lambda_1}^{\lambda_2} I_\lambda d\lambda \quad .$$

Note that the number densities and partition functions cancel in the ratio, since both spectral features are emitted by the same species.

The sensitivity of the ratio of intensities to temperature is found by taking the derivative of the intensity ratio with respect to temperature, and rearranging the expression to give,

$$\frac{\Delta R}{R} = \frac{E_1 - E_2}{k\ T_e} \frac{\Delta T_e}{T_e} \quad , \tag{16}$$

where $R = I_2/I_1$ For the two most commonly observed transitions of atomic oxygen at 7773 and 8446 Å, the sensitivity term $\Delta E/kT_e = 2880/T_e$. At temperatures above 6000 K, this ratio will be less than .5 and large changes in T_e will produce only small changes in the measured ratio. Greater sensitivity to temperature occurs with larger energy differences between emitting levels. Often, a compromise must be reached between the enhanced temperature sensitivity of higher energy levels and signal-to-noise ratio. In this regard, spectroscopic diagnostics are no different from ordinary laboratory instrumentation.

To overcome the low temperature sensitivity that arises from small energy differences between emitting levels, spectrally integrated signals from multiple transitions are used to develop a Boltzmann plot for a particular species. By taking the natural log of Eq. (14), an expression that represents the Boltzmann plot mathematically is obtained,

$$\ln\left(\frac{I}{A_{ul} g_u h \nu_{ul}}\right)_i = \frac{-1}{kT_e}(E_u)_i + C \quad , \tag{17}$$

where C contains the terms that are common to all the transitions. Temperature is then obtained from a least squares linear fit to the data and the precision of the measurement improves with the number of transitions used, provided that the energy levels and spontaneous emission rates, A_{ul}, are known accurately.

Molecular Spectra - Emission from molecular species is typically comprised of overlapping spectral features from multiple energy levels that are less completely resolved, as seen in the band structure at shorter wavelengths in Fig. 2. Despite the spectral overlap, similar analytical approaches can be used to determine temperature values. These approaches also involve taking ratios of spectral features that are reasonably well defined. Specific approaches for determining vibrational and rotational temperatures from molecular spectra have been developed by Laux[9] and Park et al[14]. The methods of Park are shown graphically in Figs. 3 and 4. The figures show emission spectra from vibrational bands of the N_2^+ (1-) system and the shaded regions indicate the spectrally integrated areas used to determine temperatures. Approximate analytical expressions for vibrational and rotational temperatures as functions of these intensity ratios are derived below. For the derivations, it is assumed that: vibrational and rotational modes are in thermal equilibrium (but $T_v \neq T_r$ is allowed); the radiation field is emission dominated; effects of nuclear spin on degeneracy are ignorable; and the individual ro-vibrational transitions are fairly isolated spectrally (in reality, the spectral resolution of the detecting instrument convolves contributions from multiple transitions, as discussed below). Also, each derivation makes use of the Born-Oppenheimer approximation to separate the electronic, vibrational, and rotational contributions to the spontaneous emission rate, which can then be written as[15]

$$A_{ul} = c\nu^3 R_e^2 q_{v_u v_l} \frac{S_{J_u J_l}}{(2J_u + 1)} \quad , \tag{18}$$

where c represents the group of constants, R_e is the electronic transition moment, $q_{v_u v_l}$ is the Franck-Condon factor, which represents the vibrational band strength, and $S_{J_u J_l}$ is the Hönl-London factor, or rotational line strength.

Vibrational Temperature - For vibrational temperature, spectrally integrated intensities near two band heads, (1,2) and (0,1) are ratioed. The two spectral regions are shown on Fig. 3, and the difference in upper state vibrational quantum number gives a difference in energy level analogous to the explicit ΔE for the two-line electronic temperature measurement that was discussed above. Emission at the vibrational band head is comprised of contributions from a number of rotational transitions, and the spectrally integrated

intensity for each band head is

$$I_i = \int_{\lambda_{i1}}^{\lambda_{i2}} I_\lambda d\lambda = \frac{cnh\nu^4}{4\pi} R_e^2(q_{v_u v_l})_i \left(\frac{n_{vi}}{n}\right) \sum_{Ji} \frac{(S_{J_u J_l})_i}{(2J_u+1)_i} \frac{n_{Ji}}{n} \quad , \tag{19}$$

where $i = 1, 2$. The ratio of the two intensities obtained from the spectral integration of the emission at the two bandheads is then

$$\frac{I_2}{I_1} = \frac{(q_{v_u v_l}\nu^4)_2}{(q_{v_u v_l}\nu^4)_1} \frac{e^{-v_2\theta_v/T_v}}{e^{-v_1\theta_v/T_v}} \frac{\sum_{J_2}(S_{J_2 J_l})_2 e^{J_2(J_2+1)\theta_r/T_r}}{\sum_{J_1}(S_{J_1 J_l})_1 e^{J_1(J_1+1)\theta_r/T_r}} \quad , \tag{20}$$

where the Boltzmann expressions for vibrational and rotational distributions have been used and the vibrational and rotational temperatures are explicitly identified. Ideally, if the rotational transitions comprising the sum for each band head had the same range of J values, then the intensity ratio would be insensitive to rotational temperature. In practice, this is not achieved, and although the rotational temperature sensitivity can be minimized, an iterative solution is required that includes a concurrent, but separate, determination of rotational temperature.

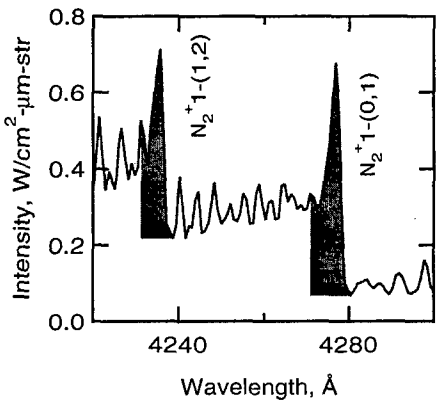

Fig. 3. Spectral integrals used to determine T_v.

The above intensity ratio can be rearranged and solved for vibrational temperature,

$$T_v = \frac{(v_1 - v_2)\theta_v}{\ln\left[(I_2 q_1 \nu_1^4)/(I_1 q_2 \nu_2^4 f(T_r))\right]} \quad . \tag{21}$$

The sums of rotational terms, which do not cancel in the ratio, are now represented by $f(T_r)$. As with the electronic temperature, the greater the difference in vibrational energies of the two levels, the greater the sensitivity to temperature.

Rotational Temperature - By taking the ratio of two spectrally integrated intensities that contain different rotational transitions, but arise from a single vibrational band, the rotational temperature can be determined. One approach is shown schematically in Fig. 4, where the ratio of the two spectrally integrated regions gives

$$\frac{I_2}{I_1} = \frac{\sum_{J_2}(S_{J_2 J_l}\nu^4)_2 e^{-J_2(J_2+1)\theta_r/T_r}}{\sum_{J_1}(S_{J_1 J_l}\nu^4)_1 e^{-J_1(J_1+1)\theta_r/T_r}} \quad , \tag{22}$$

and all common terms have been canceled. Note that this is again an idealized case, since in practice the integrated intensities include signal contributions from adjacent vibrational band transitions and from other species. In Fig. 4, the merging of spectral features caused by finite slit resolution is evident, and contributions from other radiative transitions are evident in the nonzero baseline level at the edge of the band head near 3917 Å.

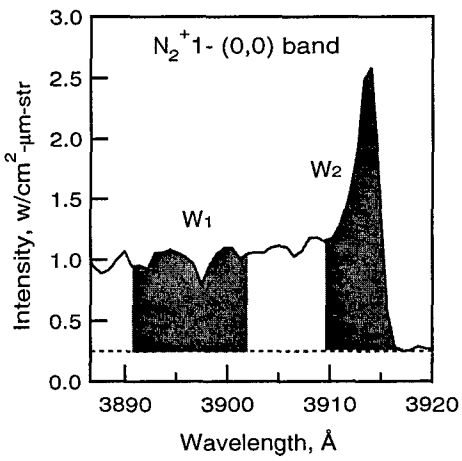

Fig. 4. Spectrally integrated regions used to determine T_r.

To illustrate the temperature sensitivity of the above relation, average values, $\overline{S_{JJ}}$ and $\overline{J}$,can be defined such that

$$\sum_{J=Ja}^{Jb} S_{JJ_l} e^{-J(J+1)\theta_r/T_r} = (\Delta J_{ab}+1)\overline{S_{JJ}} e^{-\overline{J}(\overline{J}_1)\theta_r/T_r} \quad . \tag{23}$$

With the average rotational strength and quantum numbers, the expression for rotational temperature becomes

$$T_r = \frac{(\overline{J_1}(\overline{J_1}+1) - \overline{J_2}(\overline{J_2}+1))\theta_r}{\ln\left[(I_2\overline{S_{JJ}}_1\nu_1^4)/(I_1\overline{S_{JJ}}_2\nu_2^4)\right]} \quad . \tag{24}$$

This result is analogous to the two previous derivations for determining vibrational and electronic temperatures from the ratio of spectrally integrated intensities. Here however, it is the difference in rotational energies that determines the rotational temperature sensitivity of the intensity ratio. As before, greater sensitivity to temperature is found for larger differences in rotational quantum numbers and the same considerations apply regarding a trade between sensitivity and signal level.

For all of the temperature determinations above, it is assumed that the gas is optically thin. If this is not the case, then self-absorption, or radiative trapping, must be considered. To interpret emission spectra emanating from an optically thick gas, a radiative transport model, such as NEQAIR, is required. An iterative procedure must be used to interpret and correct the spectra for self-absorption, since the absorbing populations depend on density and temperature in the same manner as the emitting populations (see Eqs. (9) and (10)). Some modeling must also be done to properly account for the coupling between rotational and vibrational temperatures for molecular spectra and for finite instrument resolution.

Species Densities - Species concentrations that are integrated along the line-of-sight can be estimated if the electronic temperature is known from one of the methods outlined above. This implies that the population of the excited electronic state is in Boltzmann equilibrium with the ground state. By rearranging the spectrally integrated form of Eq. (13), the line-of-sight integrated concentration of an atomic species in an emission dominated radiation field can be expressed as

$$nL = \frac{I 4\pi Q}{g_u A_{ul} h\nu_{ul}} e^{E_u/kT_e} \quad . \tag{25}$$

Owing to the exponential dependence of density on electronic temperature, small uncertainties in electronic temperature cause large uncertainties in the nL product. The temperature uncertainty contribution to the nL uncertainty is amplified by the factor E_u/kT_e, where E_u is the energy of the emitting level. To illustrate this aspect, consider an electronic temperature of 10000 K and the 7773 Å transition of O, which has an average upper state energy of 86630 cm^{-1} (from Wiese et al[16]). In this case $E_u/kT_e = 12.5$. Thus, integrated species density values will be considerably more uncertain than temperatures.

Abel Inversion The path-integrated nature of emission measurements limits the amount of information that can be obtained from the flow. This is a serious drawback to emission-based property measurement since typical flow situations involve spatial gradients; they are not simply one-dimensional. However, if the flow gradients are axisymmetric and emission spectra are recorded from multiple spatial locations, then an Abel inversion of the recorded signals can yield localized emission intensities.

In an optically thin gas, the radiation intensity measured by an observer is an integrated sum of volumetric emission that varies with lateral displacement, x, of the viewing line. In Fig. 5, a cross section of the axisymmetric flow under consideration is shown. The measured integrated intensity $I(x)$ is an Abel transformation of a radial distribution of emissive intensity $E(r)$

$$I(x) = 2 \int_x^R \frac{E(r) r dr}{\sqrt{r^2 - x^2}}. \tag{26}$$

The reverse of this transformation, i.e., the Abel inversion, relates $E(r)$ to the measured intensity $I(x)$:

$$E(r) = -\frac{1}{\pi} \int_r^R \frac{(dI/dx) dx}{\sqrt{x^2 - r^2}}. \tag{27}$$

If the radiating flow region is axially symmetric, then even-power polynomials can be used to represent $E(r)$ and $I(x)$, thereby simplifying the analysis. Further information on the Abel inversion can be found in Refs. 9 and 17.

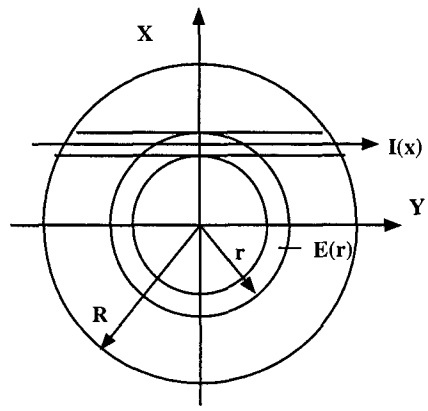

Fig. 5. Cross section of axially symmetric , optically thin radiation source.

Flow properties derived from emission spectroscopic measurements in large-scale arcjet facilities are discussed below. The discussion is organized by arcjet flow region, beginning with the arc column and ending with the shock layer over a blunt-body test article. Specific measurement examples, including experimental configuration and analysis details, are given for each flow region.

2.2 Arc Column & Electrode Package

Although optical access is limited, acquisition of emission spectra from the arc heater and electrode region can give a direct indication of the total flow conditions. Pressures are relatively high in this region, typically greater than atmospheric, and despite the high temperature, the collision frequency should be sufficient to ensure that the flow is in thermochemical equilibrium. If this is the case, then an optical measurement of temperature along with a concurrent pressure measurement would uniquely determine the total flow enthalpy. Numerical simulations of arcjet facilities often start with assumed equilibrium conditions in the electrode package region and then model the nozzle flow to calculate test conditions in the free stream. Knowledge of the flow properties in this region could specify

the input parameters and thereby enable a better evaluation of nonequilibrium, expanding flow simulations. This reasoning has motivated several investigations of arc-column and electrode package emission.

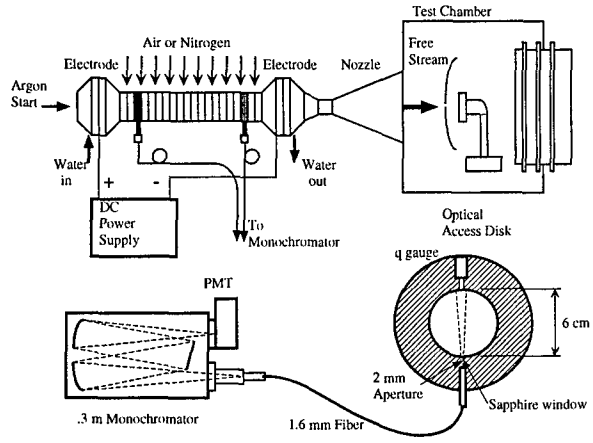

Fig. 6. Experimental setup for arc column emission measurements.

One of the earlier investigations involved the installation of a window on different segments of an arc column at AEDC.[18] The visual characteristics of the discharge were studied over a range of facility operating conditions for several locations along the column. Later, a heater segment disk with fiber-optic access was developed at Ames Research Center for installation in an arc column.[19] Using a fiber-based light collection system similar to the one that will be discussed in more detail below, Terrazas-Salinas et al[20] acquired emission spectra from the disk when it was installed in a 20 MW constricted-arc heater at two locations on the column, as shown in Fig. 6.

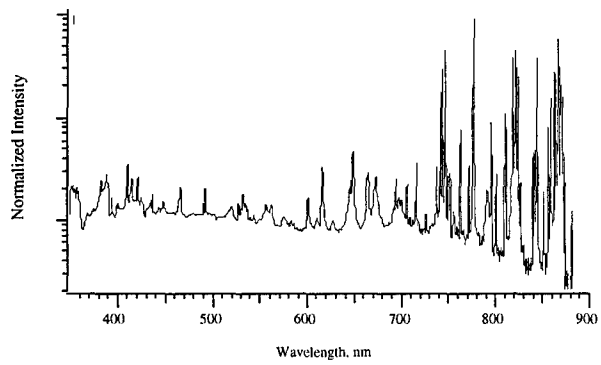

Fig. 7. Typical emission spectrum from cathode end of arc column.

A typical emission spectrum from the arc column is shown in Fig. 7. The spectrum is dominated by atomic lines with some N_2^+ ion emission seen at the shorter wavelength region where fiber attenuation begins to limit signal collection. Treating the gas as optically thin, Boltzmann plots of the atomic transition intensities were used to estimate electronic temperatures for O and N and these were compared with predictions from a numerical model of the flow in the constrictor section[21] and NEQAIR.

More recently, a series of investigations into emission from the downstream electrode region of a constricted arc heater were conducted at Johnson Space Center in their 10 MW arc heater.[22] Again, a fiberoptic collection system was used to bring the light to a spectrograph and the emission spectra were analyzed to infer electronic temperatures assuming that the gas was optically thin. A wide disparity between electronic temperatures derived from O and N transition intensities was noted for these measurements. Although the authors attributed the disagreement between the two temperatures to uncertainties in transition probabilities for N,[23] it is also possible that the assumption of an optically thin gas is inappropriate, since there will be some population in absorbing electronic states if the plenum region is filled with hot gas. It is also possible that nitrogen and oxygen are not completely mixed since they are injected separately in the Johnson arcjet. More recently, this group has acquired plenum region spectra along multiple lines-of-sight in an attempt to resolve the radial intensity gradients that are most likely present.[24]

Each of these investigations invoked the assumption that the gas was optically thin in the interpretation of the spectra. While this may be reasonable in the arc column, it may not be appropriate in the electrode package, or plenum, region. This question of self-absorption was explicitly considered in a recent investigation of electrode package emission in a 20 MW arcjet facility at Ames Research Center.[25] Findings from a preliminary analysis of the data are discussed below.

2.2.1. Experimental Configuration for Electrode Package Measurements

The current investigation of plenum radiation involves the use of a spacer disk in the electrode package to provide optical access to the flow. Based on the design of similar disks for the constrictor section,[19] this particular disk was sized to fit within the downstream electrode package and to accommodate a pressure tap and a heat transfer gauge in addition to the optical fiber. Figure 8 shows the location of the fiber view port in the downstream electrode package along with the optical layout for the experiments. The tests that are discussed below were conducted in the Ames 20 MW AHF Arcjet Facility that was described in the introductory section.

Hot gas emission from the plenum was collected through a sapphire window in the optical disk and imaged onto a 0.94 mm diameter, 30 m long, fiberoptic cable. The fiber, which delivered the light to a monochromator in a remote laboratory, was recessed

from the inside surface of the disk and viewed the emitting gas through a 2 mm aperture. A fused silica lens assembly was used to couple the fiber output with f-number matching to a 0.32 m scanning monochromator with a PMT mounted at the exit slit. The monochromator was equipped with a 1200 line/mm holographic grating blazed at 250 nm and the entrance and exit slits where both set at 50 μm. To cover the 2000 to 9000 Å spectral range during a single facility run, the monochromator was scanned at 1800 Å/min. Measured signals were converted to absolute intensities by determining the spectral response of the light collection system using standard tungsten and deuterium lamps. Further details about the optical instrumentation can be found in Ref. 25.

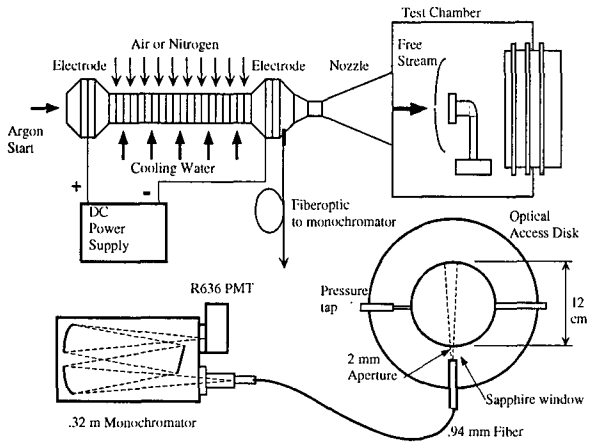

Fig. 8. Experimental setup for electrode package emission measurements.

During the facility tests PMT signals showed strong temporal fluctuations, on the order of +/- 30 %, across the spectrum. To reduce the fluctuations in the measured signals the PMT output was filtered with a 30 Hz, 12 dB/octave low pass filter. The combination of monochromator scan rate and electrical low pass filtering caused an artificial broadening (the Full-Width at Half-Maximum (FWHM) increased from 2 to 2.6 Å) and slight skewing of the line shapes. The settings chosen were considered necessary to reduce the rapid fluctuations and still scan over the desired wavelength range during a 4 min facility run. Integrated line intensities, which were used in the data analysis, were negligibly affected.

Test gases were either air/argon or N_2/argon mixtures and measurements were performed over a wide range of facility operating conditions. A compilation of the test conditions is given in Table I of Ref. 25. Results from a preliminary analysis of some of the data are discussed below.

2.2.2. Electrode Package Results and Discussion

The raw signal from a typical spectral scan recorded during a single facility run is shown in Fig. 9a. This raw signal was then corrected for the instrumental spectral response that was determined from the tungsten and deuterium lamp calibration, which is shown in Fig. 9b. The resulting calibrated, absolute intensity is shown in Fig. 9c and the predominance of atomic line emission over molecular band emission is evident. Despite differences in relative strengths stemming from different thermodynamic conditions, the spectral features seen in Fig. 9c are the same as seen in the spectrum from the arc column that was presented in Fig. 7. Assignments of some of the more important spectral features of the electrode package spectrum are given in Fig. 2 for an expanded wavelength scale.

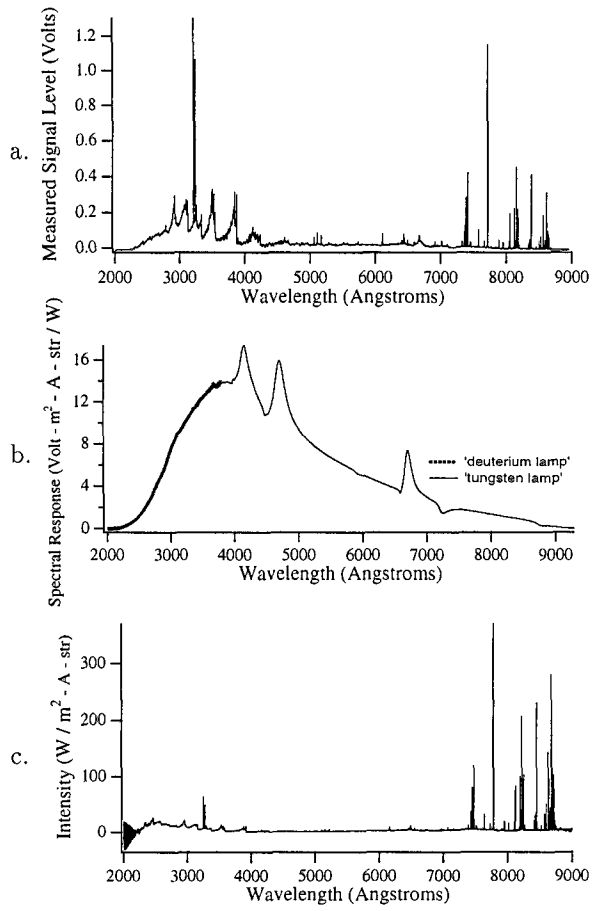

Fig. 9a-d. Example emission spectrum from electrode package measurements showing: a, raw signal from electrode package; b, system spectral response; and c, calibrated emission spectrum.

Using the basic procedure outlined in the introductory section, Boltzmann plots of the spectrally integrated atomic transition intensities were constructed to determine electronic temperatures assuming that the flow region was in local thermal equilibrium. NEQAIR simulations were performed to evaluate self-absorption since it is possible that hot gas entirely fills the electrode package region. Example Boltzmann plots for N and O are shown in Fig. 10 for a single facility test. Two plots are shown for each species; one assuming the

gas is optically thin, and a second plot with signals corrected for radiation trapping based on NEQAIR simulations of the radiative transport. Instead of assuming an arbitrary temperature profile within the electrode package, the simpler assumption of uniform conditions over the measurement domain was made. Note that the correction for self-absorption improves the agreement between the electronic temperatures that were determined from the slopes of the N and O distributions.

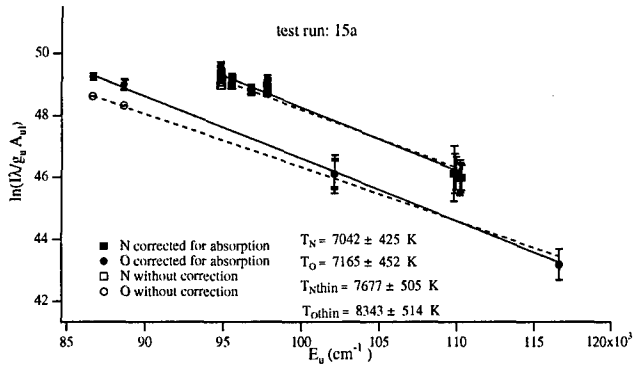

Fig. 10. Example Boltzmann plots for N and O, with and without correction for self-absorption.

Electronic temperatures deduced from O and N intensities are presented in Fig. 11 as a function of specific heater energy ($= VI/\dot{m}$) for a range of test conditions. Two sets of temperatures are shown for each condition: with and without correction for self-absorption. The temperatures show little variation as heater power (VI) is increased. Agreement between the electronic temperatures determined from O and N transitions is consistently better when self-absorption from a uniform absorber distribution along the line-of-sight is taken into account. Also, the temperature values derived from the absorption corrected intensities are consistently lower than the uncorrected values.

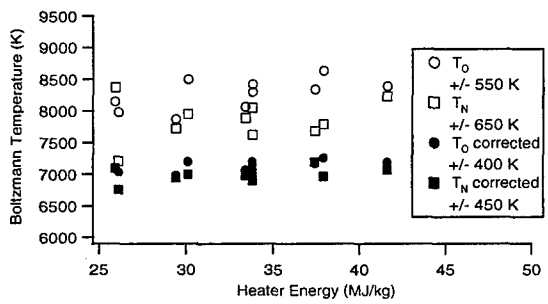

Fig. 11. Plenum temperatures derived from the analysis of the emission spectra for 2.4 atm pressure.

Despite the relatively low signal levels, the molecular band emission was also analyzed for rotational and vibrational temperature using the approach of Park[14], which was based on spectrally-integrated intensities of N_2^+ (1-) band features. Values of T_r that were obtained from the analysis were compared with T_e values and were found to be consistently higher for all test conditions. Vibrational temperatures that were determined from the spectrally integrated intensity ratios were even higher and appeared to be unreasonable. All of the temperature values were determined from spectra that were corrected for self-absorption assuming that the thermodynamic conditions and species distributions were uniform across the viewing region. This assumption may not hold for all species; in fact, it is possible that the molecular species are absent near the center of the flow where the absorbing atomic populations may be greatest. Likewise, the excessively high vibrational temperatures may indicate that the band populations may not be equally distributed along the line of sight. However, the possibility of nonequilibrium conditions can not yet be ruled out.

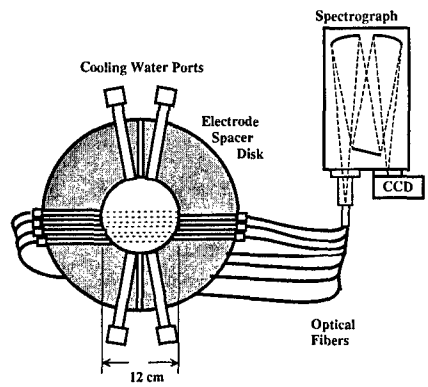

Fig. 12. Multiple line-of-sight optical disk for electrode package emission measurements.

Interpretations of emission spectra from the electrode package and plenum regions are severely constrained by a lack of knowledge about spatial gradients in flow properties and species distributions that may exist. To gain further insight, an improved optical disk with multiple line-of-sight detection capability has been fabricated for installation as a spacer disk in the electrode package of the 20 MW arcjet facility. The arrangement of the seven viewports is shown in Fig. 12 and the assumption that the flow is, on average, axisymmetric has been exploited in the design.

Measurements in the electrode region are still in the development stage at this time. There is not yet sufficient information to definitely establish the existence of thermal equilibrium within the electrode package, and the question of chemical equilibrium has not been attempted. Consequently, the impact of electrode package and arc column emission measurements on arcjet flow modeling is currently negligible.

2.3 Nozzle and Free Stream

In most large-scale arcjet facilities, optical access exists at the exit of the nozzle, which is usually attached to an enclosure where material tests are conducted.

Provided that populations in excited electronic levels exist, it is possible to acquire emission spectra from the free stream at the entrance to the test chamber. Normally, one would expect little or no population in excited states based on credible estimates of stream temperatures and the widely held belief that the flow is thermally and chemically frozen for most test conditions. However, if excited state populations exist, then it may be possible to use emission spectroscopy to assess the degree nonequilibrium of the free stream.

As part of an earlier spectroscopic investigation of the Ames AHF Arcjet Facility, Gopaul[26] recorded emission from the γ $(A^2\Sigma^+ - X^2\Pi)$ and δ $(C^2\Pi - X^2\Pi)$ systems of NO in the free stream. Only rotational transitions from the lowest vibrational level of the two electronic states were detected. Using NEQAIR simulations to fit the vibrational bands by varying the rotational temperatures, values of rotational temperatures for several free stream test conditions were obtained. Since no emission was measured from levels having $v' > 0$, no assessment of the free stream vibrational temperature could be made (recall that emission from two different vibrational levels is required to determine vibrational temperature). With the assumption that the upper electronic state population was in Boltzmann equilibrium with the ground state, large NO (X) populations in the free stream were inferred from the measurements. Additional CFD simulations of the nozzle flow were conducted to attempt to understand the NO populations.[27] As will be discussed below in the section on LIF measurements, it is likely that the NO (X) state is not in equilibrium with the A and C electronic states.

In more recent measurements with a different nozzle and with different facility operating conditions, Park et al [14,28] reconfirmed the findings of Ref. 26 regarding the emitting states and vibrational levels of NO. Surveys over a wide wavelength range with long accumulation times on a CCD camera gave no indication of appreciable excited state populations for other species in the free stream flow. However, this does not rule out possible populations in metastable electronic states such as N_2 (A), O (^1S) and (^1D), or N $(^2D^\circ)$ and $(^2P^\circ)$. In a second experiment, the radial distribution of excited-state NO was investigated in the free stream flow.[29] These investigations and their findings are discussed below.

2.3.1 Experimental Configuration for Free-Stream Measurements

A typical optical configuration for the free steam measurements is shown in Fig. 13. The spherical collection mirror was positioned to give an object to image magnification of 0.25 and a mask with eight apertures was used to image eight separate (about 3 mm apart) 0.2 mm x 0.5 mm object areas in the flow onto a CCD camera. The spatial dimension of the camera could be aligned with either the flow axis or the spanwise (radial) direction of the conical flow.

The spectrograph was equipped with a 1200 g/mm, 300-nm-blaze ruled grating and the entrance slit width was set to 50 μm. This produced a reciprocal linear dispersion of 3 nm/mm. Emission spectra were captured by a 1024×256 2-D CCD camera array mounted at the exit plane of the spectrograph with the 1024 pixel side in the wavelength direction. The 27 μm square pixels limited the spectral coverage of the array to approximately 800 Å and the total spatial coverage to roughly 25 mm. The spectral resolution on the array and instrumental broadening were determined to be 0.8 Å/pixel and 1.6 Å FWHM, respectively.

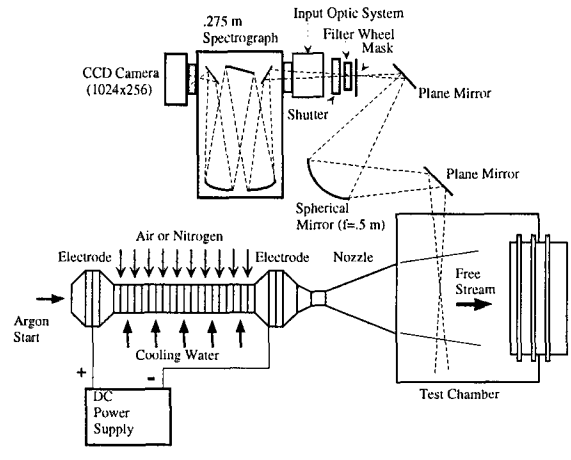

Fig. 13. Experimental setup for free stream emission measurements.

Calibration of Optical System The measured emission spectra were corrected for the spectral response of the mirrors, filters, grating, and CCD array. Two National Institutes of Standard and Technology (NIST) traceable standards of spectral radiance, a deuterium lamp and a tungsten ribbon-filament lamp, were used to calibrate the optical system in units of $W/cm^2 - \mu m - sr$. Details of the procedure are given in Ref. 14.

Facility For these tests, the arcjet nozzle was configured with a 3.81 cm diameter throat and an exit diameter of 30.48 cm. The arc heater was operated at two different test conditions that are identified as the low pressure and high pressure cases. For the low and high pressure cases the heater pressure, arc current, and arc voltage were: Low) 1.7 atm, 1141 A, and 2657 V and High) 6.8 atm, 2075 A, and 5630 V; respectively. The test gas consisted of air and argon ($\dot{m}_{Ar}$ =.03 kg/s).

2.3.2 Free Stream Results and Discussion

A typical free stream emission spectrum for the 2000 to 2800 Å grating position is shown in Fig. 14. This spectrum was taken on the free stream centerline, and

is representative of the eight separate spectra acquired by the CCD-based system. As mentioned in the introductory section, only emission from $v' = 0$ levels was evident for both the γ and δ bands. As indicated in Fig. 14, the detected spectra were identified as belonging to the NO γ and δ systems.

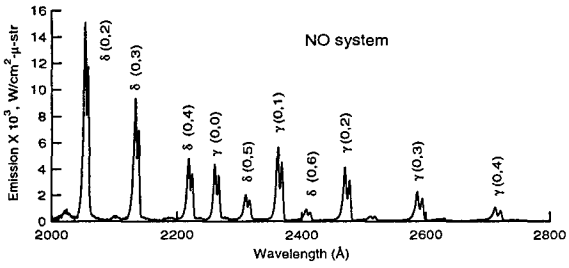

Fig. 14. Free stream spectra taken at the center of free stream and 30 cm downstream from the nozzle exit.

The rotational temperature, T_r was determined from the well resolved vibrational bands in Fig. 14. The FWHM of the band intensity was calculated for different T_r values using NEQAIR. In Fig. 15, the FWHM of the NO γ (0,1) band is plotted as a function of T_r with a fixed instrumental line width of 1.6 Å. Using this correlation and the measured FWHM of the NO γ (0,1) band, a T_r value was obtained for each test condition for the eight spectra along the flow axis.

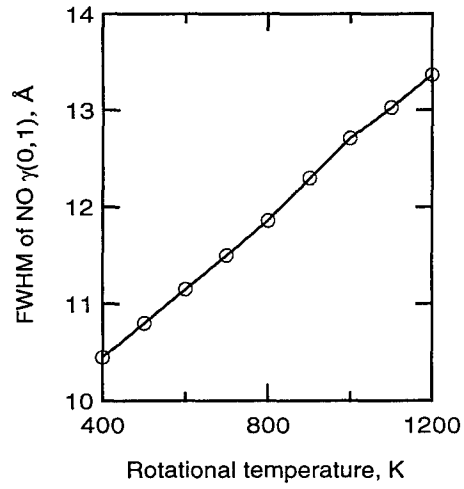

Fig. 15. FWHM of NO-γ (0,1) band as a function of T_r.

Rotational temperatures for two different facility operating conditions are summarized in Table I along with the facility operating conditions for the tests. The reported values represent the average of the three rotational temperatures determined from the NO γ (0,1), (0,2), and (0,3) features. As expected, the rotational temperature from the higher pressure, higher current test case is greater than that for the lower pressure and current case. Because the T_r determination does not rely on absolute intensity, the leading contribution to the uncertainty comes from unresolved background emission underlying the NO spectral features rather than uncertainty in the intensity calibration. The cause of this background emission has not been identified. Although the level of this background signal is small, it does affect the temperature determination. A secondary contribution stems from the finite spectral resolution and its influence on the determination of the FWHM. This contribution was quantified by evaluating the scatter in the eight separate free stream measurements that were simultaneously acquired by the CCD camera. Thus, the uncertainty value indicated in the table includes both contributions.

Table I. Arcjet test conditions and measured rotational temperatures from free stream emission experiments.

Run Condition & Rotational T				
Run	Pressure	Current	Voltage	Temp.
	atm	A	V	K
A	1.70	1141	2657	618±38
B	6.80	2075	5630	989±75

It should be noted that the T_r values given in Table I represent line-of-sight intensity averaged values for the free stream. Thus, the distribution of the NO emission in the stream must be relatively uniform for the T_r values to be representative of the free stream.

Radial Distribution of NO γ- To ascertain the distribution of the NO emission in the free stream, a radial intensity survey was performed. For this experiment, the image was rotated 90° to align with the radial, or spanwise, direction and a modified mask was used to define four object areas separated by 8.9 mm in the flow. By tilting the first plane mirror of the collection system, four spatially distinct spectra were acquired at 6 locations spaced at 35.6 mm apart to cover the stream during a single run.

Results from the radial survey of the NO emission are shown in Fig. 16 for the low pressure, low current condition. Peak values of NO γ (0,2) band emission are plotted as a function of radial distance for one of the four object areas that were imaged at each measurement location. Also shown on the figure is an Abel-inverted emission distribution derived from the radial measurements. As this shows a large, relatively uniform region in the central portion of the flow, it appears that the T_r of NO γ and δ states is representative of a large portion of the inviscid flow. Whether or not the rotational temperature of these excited NO states represents the rotational temperature of the ground state molecular populations has not yet been established.

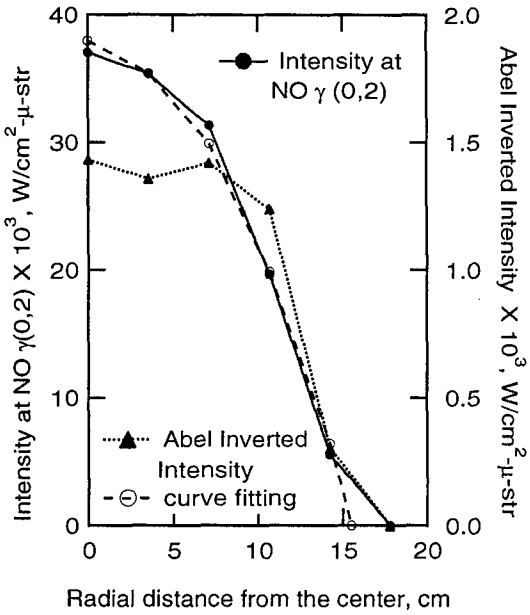

Fig. 16. NO γ (0,2) intensity as a function of radial position.

Based on the results of these and earlier investigations, it appears that measurements of free stream rotational temperature can be made with relatively low uncertainty. This presents opportunities for instrumentation development that can enable real-time monitoring of the free stream rotational temperature with a small, dedicated spectrometer and detector.

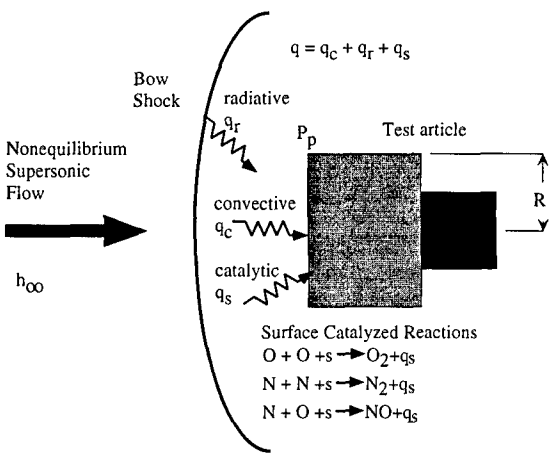

Fig. 17. Stagnation point heating configuration for a blunt-body test article.

2.4 Shock Layer Flows

A stagnation point heating configuration is frequently used in the development and testing of thermal protection materials in large scale arcjet facilities. With the stagnation point configuration and a supersonic free stream flow, a bow shock is formed over the test article, as depicted in Fig. 17. Flow compression by the shock causes a significant temperature rise, which populates many emitting states. For modest enthalpy levels, significant visible emission can be observed emanating from the shock layer. Thus, the potential use of shock-layer emission to characterize the flow has been investigated extensively.[3,28–34] Although similar investigations of subsonic boundary layer flows formed over blunt bodies have also been undertaken,[35,36] the discussion in this section will be restricted to shock layer measurements.

Characterization of the shock layer enthalpy by spectral analysis of emission measurements is possible if equilibrium conditions are reached within the shock layer. If equilibrium is attained, then the spectral features of radiation are a function only of pressure and enthalpy. Pressure measurements in the shock layer are routinely performed, as mentioned in the introduction. If a spectral measurement of temperature can be obtained under equilibrium conditions, then the flow enthalpy can be specified.

In recent shock layer emission experiments carried out at the Ames AHF Arcjet Facility, tests were conducted at conditions deemed likely to generate a region of thermochemical equilibrium within the shock layer; i.e., at higher stagnation pressure and with a large diameter test model.[14,28,29] In these experiments, spectrally resolved emission measurements were acquired simultaneously from multiple spatial locations along the central stagnation streamline for two different facility operating conditions. Analytical methods were developed to determine T_r, T_v, and T_e of the shock layer using the N_2^+ 1- system and atomic oxygen lines. For one test condition, the spectrally determined temperatures were used to obtain line-of-sight averaged number densities of N_2^+, N_2, CN, and O from the shock layer emission spectra. An additional experiment was performed to evaluate the extent and influence of radial intensity gradients for the low pressure, low current condition. The experimental configuration, analytical approach, and flow property measurement results for these investigations are discussed below.

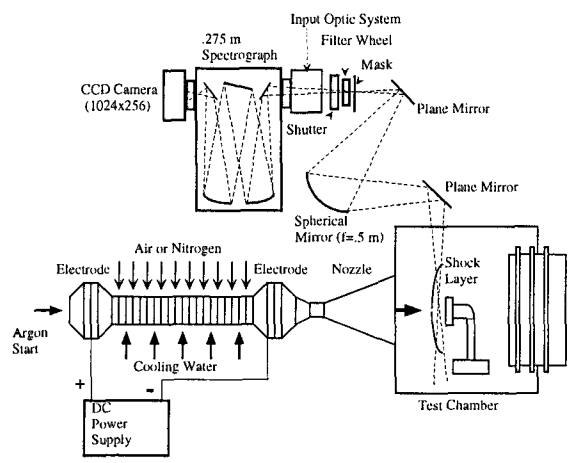

Fig. 18. Optical configuration for shock layer emission measurements in the AHF Arcjet Facility.

2.4.1 Experimental Configuration for Shock-Layer Measurements

For the shock layer investigations, the experimental configuration is basically the same as that given above for the free stream emission measurements. However, a 15.24 cm diameter blunt-body test article is placed in the stream and a shock layer is formed, as shown in Fig. 18. The eight apertures of the mask are now used to define eight distinct object areas, which are spaced roughly 3 mm apart, within the shock layer. The arrangement of the aperture images in the object region is shown in Fig. 19. The total distance imaged onto the CCD camera from the shock layer was limited to 25 mm, which did not allow complete shock layer coverage in a single facility run for the test conditions. Therefore, two axial positions of the test article, 34.5 cm and 36.9 cm downstream of the nozzle exit, were used to obtain spectra from the full shock layer. Facility test conditions for these experiments were the same as given above in Table I for the free stream measurements.

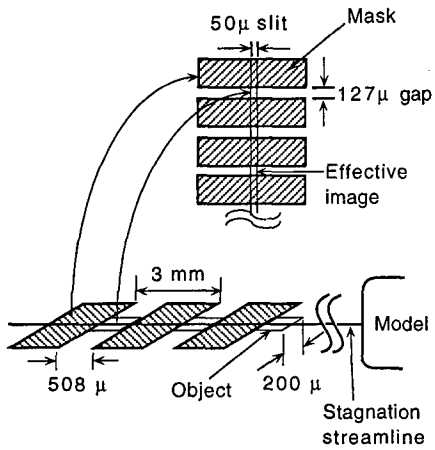

Fig. 19. Object and image planar areas defined by the mask used in the collection system for the axial shock layer survey.

2.4.2 Flow Properties from Emission

Before discussing the flow properties derived from the analysis of the emission spectra, it is useful to review a typical emission spectrum acquired at one of the eight spatial locations within the shock layer. This spectrum is shown in Figs. 20a-d, and it was acquired at a position 17.9 mm upstream from the face of the test article for a high current, high pressure test condition. In some of the figures, measured emission from multiple separate grating positions are joined.

In the 2000-3000 Å range, as shown in Fig. 20a, NO γ was the most significant with some weaker emission from higher vibrational levels of the N_2 (2+) system. Emission from the NO β system could also be present even though there is no distinct evidence of NO β spectral features.

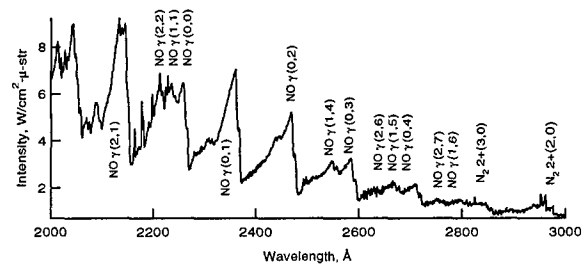

Fig. 20a. Shock-layer emission spectrum in the 2000 -3000 Å range for a flat-faced, cylindrical test article of 15.24 cm diameter.

In the 3050-3650 Å and the 3950 - 4820 Å spectral ranges, as shown in Figs. 20b and 20c, the identified transitions were attributed to NO (γ), N_2 (2+), N_2^+ (1-), and CN Violet systems. Also, several Cu atomic transitions are identified. These were expected, because copper electrodes were used in the AHF Arcjet Facility for these tests and copper is present in the stream due to arc-induced erosion.

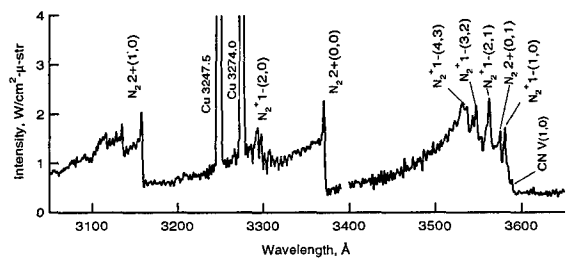

Fig. 20b. Shock-layer emission spectrum in the 3050 - 3650 Å range for a flat-faced, cylindrical test article of 15.24 cm diameter.

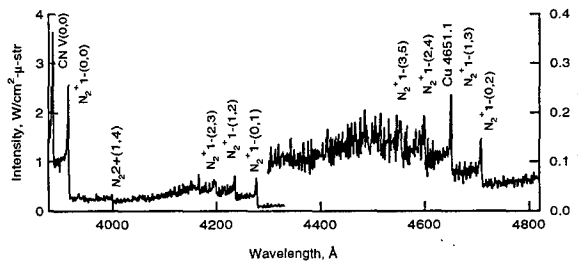

Fig. 20c. Shock-layer emission spectrum in the 3950 - 4820 Å range for a flat-faced, cylindrical test article of 15.24 cm diameter.

Example spectra for the 7500 to 9500 Å range are shown in Fig. 20d. The dominant emission features are O and N atomic lines, with a broad background contribution from N_2 (1+) emission. Transitions that were used to determine electronic temperatures within the shock layer are identified by their upper and lower electronic states.

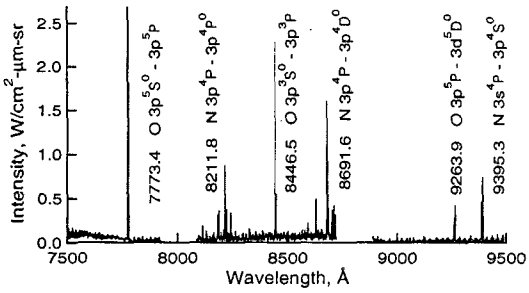

Fig. 20d. Shock-layer emission spectrum in the 7500 - 9500 Å range for a flat-faced, cylindrical test article of 15.24 cm diameter.

Temperatures from Spectra- As shown in Figs. 20b and 20c, the N_2^+ 1- band system was the most dominant one and it proved to be the most reliable for determining line-of-sight averaged values of T_r and T_v.[24] The analytical approach is based on the use of ratios of spectrally integrated intensities in well-resolved spectral regions that are largely free of interfering emission from other species. Although peak intensity ratios were also evaluated, area ratios were selected because of their reduced sensitivity to the limited spectral resolution of the CCD camera.

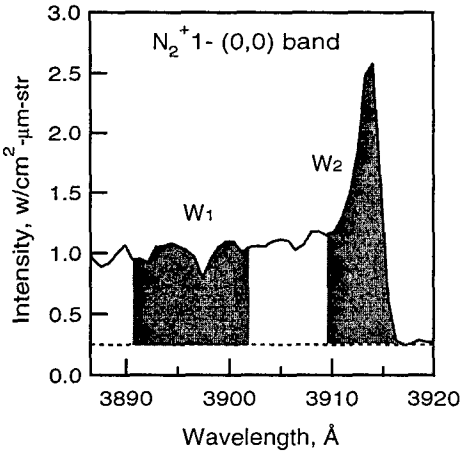

Fig. 21. A pair of areas used in T_r determination.

Rotational Temperature - In contrast to the relatively cool free stream conditions, T_r of the shock layer is quite high, and the vibrational bands are no longer completely resolved. Therefore, to evaluate T_r from the shock layer spectra, an approach based on the ratio of spectrally integrated areas within a single vibrational band was developed. Details of this analysis were presented in the introductory section above, and an approximate expression relating T_r to the ratio of spectrally integrated intensities was derived,

$$T_r = \frac{(\overline{J_1}(\overline{J_1}+1) - \overline{J_2}(\overline{J_2}+1))\theta_r}{\ln\left[(W_2\overline{S_{JJ}}_1\nu_1^4)/(W_1\overline{S_{JJ}}_2\nu_2^4)\right]} \quad .$$

In Fig. 21, the spectral intervals W_1 and W_2 of the N_2^+ 1- (0,0) band system that were used to determine T_r are shown by the shaded regions. The baseline signal was taken from the minimum near the band head rather than absolute zero of the spectral intensity to reduce the contribution of any unresolved background light to the integrals.

While the approximate expression given above is useful for assessing rotational temperature sensitivity to changes in intensity ratios, it is not sufficiently accurate for determining T_r values. Instead, NEQAIR simulations were run to develop correlations between the intensity ratio values and T_r.[14] As an example, the ratio of integrated spectral intensities from the two regions is shown in Fig. 22 as a function of T_r and T_v. Although the intensity ratio shows some sensitivity to T_v at higher rotational temperature, it appears to be relatively insensitive to T_v over most of the range of temperatures anticipated in the shock layer.

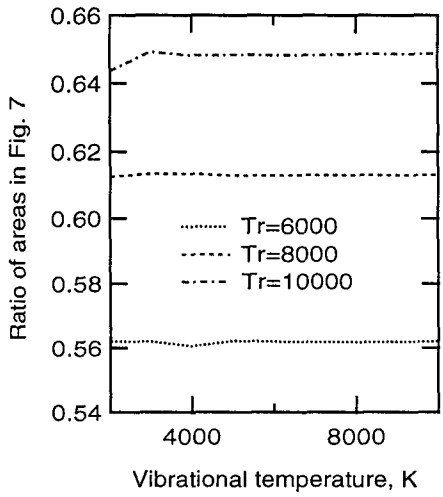

Fig. 22. The ratio of spectral integrals from the N_2^+ 1- (0,0) band as a function of T_r and T_v.

Vibrational Temperature - The determination of T_v from N_2^+ 1- system emission involves an approach similar to that used in T_r evaluation, except now the spectral integrals are taken from two different vibrational bands with $v_1' \neq v_2'$. In Fig. 23, what were determined to be the optimum intervals for this application[14] are shown by the extent of the shaded region. To maximize signal levels and permit easy identification, the intervals were restricted to the band-head spectral regions. Again, to reduce the contribution of background signal, each area was measured from the minimum close to the band head. As with T_r, the simplified analytical expression that was developed in the introductory section above to relate T_v to the measured intensity ratio,

$$T_v = \frac{(v_1 - v_2)\theta_v}{\ln\left[(I_2 q_1 \nu_1^4/(I_1 q_2 \nu_2^4 f(T_r))\right]} \quad ,$$

is only useful for evaluating differences in uncertainty for different spectral features. Accurate determination

of T_v requires the use of NEQAIR, or a similar spectral model to account for the coupling between T_r and T_v as well as possible interfering emission from other species. Using NEQAIR, correlations were developed between T_v and the spectrally integrated band intensities.

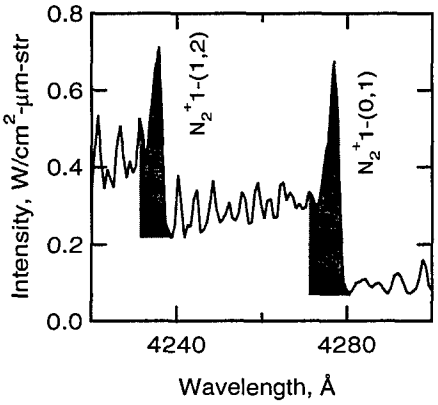

Fig. 23. A pair of areas used in T_v determination.

Electronic Temperature - Two sets of atomic oxygen transitions were used to determine electronic temperatures in the analysis of spectra from these experiments, and their wavelengths were: 1) 7773.4 and 9263.9 Å, 2) 8446.5 and 9263.9 Å. These transition pairs had adequate signal-to-noise ratios and their difference in upper-state energy levels is greater than other possible two-line combinations in this spectral region. As discussed in the introductory section on emission measurements, the uncertainty in T_e due to the uncertainty in intensity decreases as the difference in energy levels increases (see Eq. (16)). For T_e, the analytical expression that was derived in the introductory section,

$$T_e = \frac{(E_1 - E_2)/k}{\ln[(I_2 A_1 g_1 \nu_1)/(I_1 A_2 g_2 \nu_2)]} \quad ,$$

was used to determine electronic temperature values from the shock layer emission spectra. However, the influence of the unresolved background emission that underlies the atomic transitions was evaluated using NEQAIR.

Line-of-sight Integrated Species Densities - With the assumption that $T_e = T_v$ for the molecules, the integrated species densities along the line-of-sight could be determined from the relation,

$$nL = \frac{I 4\pi Q}{g_u A_{ul} h\nu_{ul}} e^{E_u/kT_e} \quad , \qquad (28)$$

which was derived by spectrally integrating Eq. (14) and solving for nL. Values of nL were obtained for N_2, CN, and N_2^+ using T_v determined from the N_2^+ band head ratios.

Uncertainty of Spectral Analysis - For the temperatures derived from emission measurements, the leading contributions to the uncertainties were typically: 1) the background signal that is thought to consist of stray light and contributions from unidentified species; 2) finite instrumental resolution of the important spectral features, which can be seen in Figs. 21 and 23; 3) coma from the off-axis reflectors in the spectrograph, which shifted the spectra in wavelength for different locations on the CCD camera; and 4) uncertainties in spectroscopic constants.

Uncertainties arising from the absolute intensity calibration are considerably smaller than the contributions listed above for temperatures because ratios of spectral features were used instead of absolute intensities. Whenever possible, ratios of spectral features from a single grating position, or, in the case of electronic temperatures, adjacent grating positions were used to minimize uncertainty contributions from the instrumental calibration. For integrated species densities, however, the absolute calibration uncertainty does contribute, but it is still less important than the uncertainty in electronic temperature (or T_v, depending on what was assumed). Possible additional uncertainty contributions from facility operation and spatial averaging are discussed below.

2.4.3 Shock Layer Results and Discussion

Results are presented for shock layer temperature and species density measurements that were derived from spectrally resolved emission emanating from multiple locations within the shock layer. All of the measured quantities represent time-averaged values obtained during the steady operation of the facility. Spectral surveys of the shock layer emission were performed for two different optical configurations. In the first configuration, multiple spectra were acquired along the central stagnation streamline for the high and low pressure flow conditions given in Table I. A different optical arrangement was used to perform a survey of the shock layer emission at the lower pressure condition of Table I to assess the radial intensity gradients within the shock layer.

High Pressure Case - Line-of-sight averaged flow temperatures for the high pressure test case are shown in Fig. 24, which presents shock layer profiles of T_r and T_v for two separate facility runs at the same nominal test conditions. Uncertainties in the measured values are indicated by error bars. For both T_v and T_r, the measurements indicate a general trend of decreasing temperature as the test article surface is approached. Agreement between the two different sets of T_v and T_r measurements is generally quite good, which indicates that the facility performance is reasonably repeatable. For each test, the line-of-sight averaged T_v and T_r values do not overlap within their estimated uncertainties; T_r is consistently higher than T_v. While this difference may indicate the absence of thermal

equilibrium, it may also be indicating the influence of differential averaging effects along the line-of-sight. This latter effect is important, since contributions to the measured intensity come from the vicinity of the shock front at all spatial locations. Near the shock, the flow is more likely to be in nonequilibrium and this nonequilibrium contribution to the line-of-sight averaged intensity may be significant. Finally, the uncertainty in T_r is greater than in T_v. This arises from the difference in sensitivities of the temperatures to the respective intensity ratios. Electronic temperatures are not shown in Fig. 24 because it was found that one of the transitions used in determining T_e, the 8446 Å transition of O, has a large, unresolved background contribution that cannot be properly accounted for in the analysis. This issue is discussed further below.

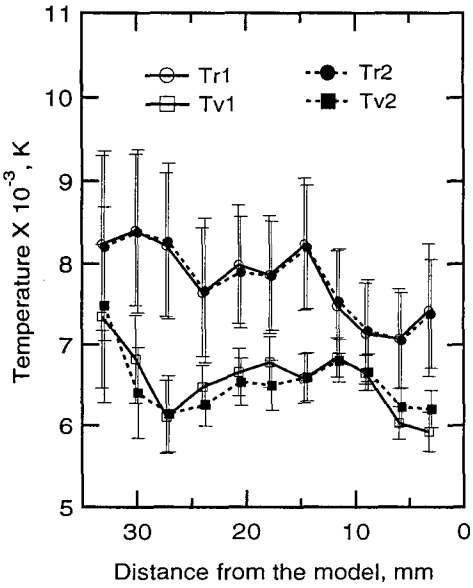

Fig. 24. Shock layer T_r and T_v profiles for the high pressure case. Note that data are shown for two different facility runs and that the flow goes from left to right. Lines are drawn to guide the eye.

Species Densities for High Pressure Case - Line-of-sight integrated species densities, nL, of N_2, CN, and N_2^+ are shown in Fig. 25 for one run of the high pressure case. The electronic temperature for these species was assumed to be equal to the line-of-sight averaged vibrational temperature that was measured using the N_2^+ intensity ratio (see Eq. (28)). All of the integrated species densities appear to increase moving from the shock front into the shock layer and then decrease as the test article surface is approached. The uncertainties are again indicated by the size of the error bars. Uncertainty is greatest for nL for N_2, owing to the use of (2+) system emission, which has a high upper state energy level, to determine the integrated density. Recall that for species densities, the uncertainty in electronic temperature is amplified by E_u/kT_e. The upper state energy levels of CN and N_2^+ are approximately half of that of the N_2 C state. Consequently, the uncertainty in $T_e = T_v$ has less impact on those species.

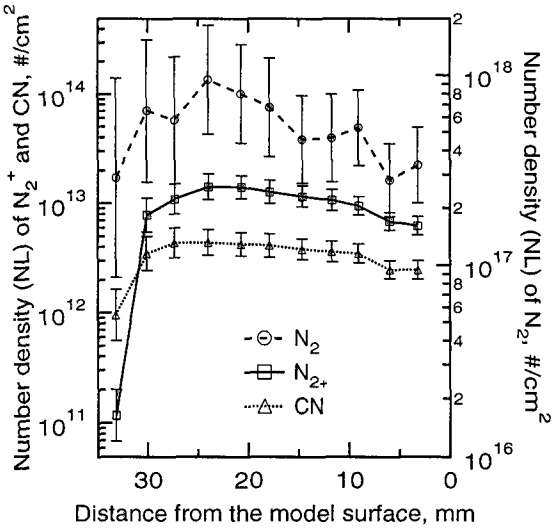

Fig. 25. LOS integrated number densities of N_2^+, N_2, and CN along the stagnation streamline.

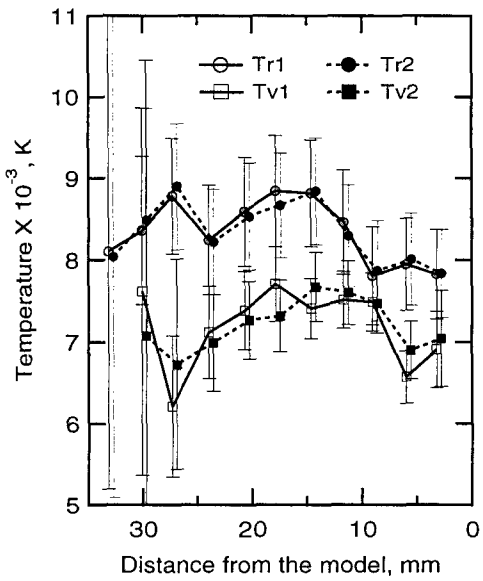

Fig. 26. Shock layer T_r and T_v profiles for the low pressure cases. Note that data are shown for two different facility runs.

Low Pressure Case - Line-of-sight integrated T_r and T_v values for the lower current, lower pressure case are shown in Fig. 26. Again, results from two different facility runs are shown, and the agreement between the measurements from the two different runs is reasonable. The agreement is generally better for the rotational temperatures and improves for the measurement locations nearer to the test article. The uncertainties are largest near the shock, owing to relatively weak N_2^+

emission signals superimposed on a larger background signal. Although T_v and T_r appear to nearly converge at 10 mm, the two temperatures do not overlap near the test article surface. As in the high pressure case, this could indicate thermal nonequilibrium, or it could indicate differential averaging effects along the line-of-sight. Further analysis of the emission has indicated that the temperatures near the shock may be less reliable owing to differences in intensities between the two separate runs.[29]

Radial Temperature Profiles - To better understand the spatial averaging of intensity within the shock layer, a radial survey was conducted at the low pressure conditions using the test article and optical components described above. However, as noted in the discussion of the free stream survey, the mask was modified to reduce the number of imaged areas to four and the image was rotated to align with the radial flow direction. For the shock layer survey, four spatially distinct spectra were acquired at intervals of 17.8 mm to cover the entire shock layer. The survey was conducted at a location 12.7 mm upstream of the test article surface. Details of the experiment are given in Ref. 29. The emission spectra that were acquired at multiple locations in the radial direction during a single facility run were analyzed by performing an Abel inversion, as described in the introductory section on emission diagnostics above. Rotational, vibrational, and electronic temperature values were then derived from the spatially resolved emission distribution using the analytical methods that were described above.

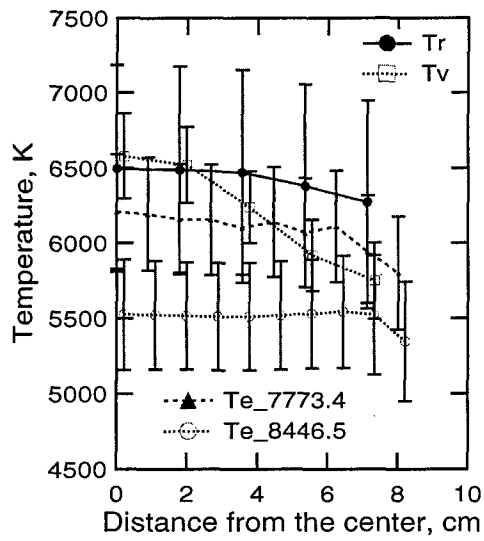

Fig. 27. Radial temperature profile in the shock layer at 12.7 mm upstream from the test article. Labels for T_e indicate the shorter wavelength O transition of the pair.

Electronic, vibrational, and rotational temperatures that were determined for each radial position for the shock-layer flow are shown in Fig. 27, where they are plotted as functions of distance from the central flow axis along the radial direction. Although the three temperatures were all measured at the same location, the values are offset slightly from each other to improve clarity. Twice as many electronic temperatures are shown, because values were determined for the first and third object areas at each location. Only the first object area was used to derive vibrational and rotational temperatures. As before, error bars for each temperature are used to indicate uncertainties. Recall that two different T_e values were determined using two sets of oxygen transitions: 1) 7773.4 and 9263.9 Å, and 2) 8446.5 and 9263.9 Å. Electronic temperatures from these transition pairs are identified by the shorter wavelength transition.

The measured temperatures presented in Fig. 27 can be seen to agree within their error bounds, except T_e based on the oxygen lines at 8446.5 and 9263.9 Å. Since this T_e is consistently lower than the value derived from the other atomic lines, it is likely that even after background subtraction there is still significant emission from other species in the spectrally integrated signal. Supporting evidence was found by comparing the inferred nL densities of atomic oxygen using the two different T_e values. The value obtained using the 7773.4 and 9263.9 Å line pair was more consistent with estimates of O densities based on the impact pressure measurement and the known oxygen mass flow.[29]

Excluding the T_e values derived from the 8446.5 Å transition pair, the three different measured temperatures agree within their error bounds, which indicates that the flow could be in thermal equilibrium. Further analysis to assess the chemical state of the shock layer flow at the measurement locations is currently underway.

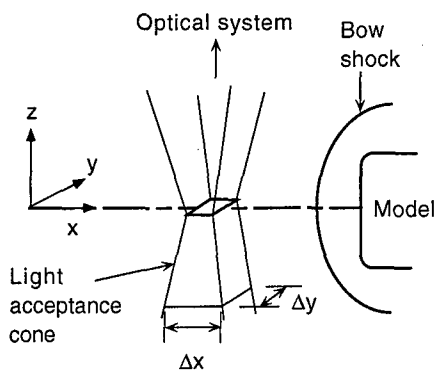

Fig. 28. Schematic representation of the light collection cone.

Spatial Averaging - In an attempt to better understand the averaging of the emission signals along the line-of-sight, a ray tracing analysis of the light collection geometry was performed for the initial f/50 experimental configuration that was used in the axial shock layer survey. The analysis indicated that the spatial

resolution of the light collection system was not what had been designed. An idealized representation of the light acceptance cone for a single object area defined by the optical components is shown in Fig. 28. In reality, the planar cross section depicted on the figure at the flow centerline is distorted by astigmatism introduced by the off-axis orientation of the spherical mirror of the collection system. Light rays in the local x and y directions are actually focused at different locations along the line-of-sight dimension because of this astigmatism.

Using ray-tracing software, the dimensions of the light collection cone were calculated at different locations along the line-of-sight and the results are shown in Fig. 29. Calculations of Δx and Δy were done from 8 cm above to 12 cm below the stagnation streamline. Separation of the focal points for Δx and Δy is apparent, and the size of the imaged area extends to roughly .28 cm for Δy and .43 cm for Δx near where the sight line crosses the shock wave. These dimensions are on the order of the shock stand-off distance for these experiments, and it is likely that additional spatial averaging along the spanwise and streamwise directions was introduced into the measurements. In view of this result, the aperture was closed further in the radial survey experiment to increase the system f/# to 100 and thereby minimize this effect.

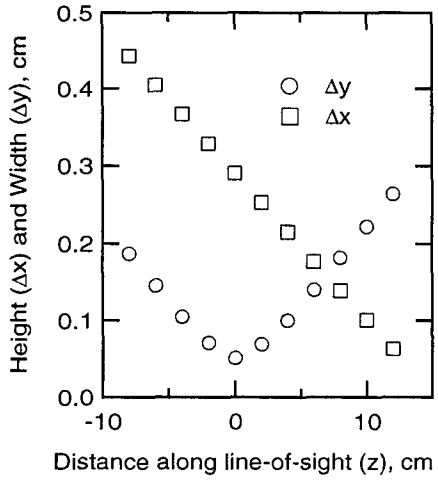

Fig. 29. Dimensions of the light cone of Fig. 28 as a function of distance along the line-of-sight direction.

Uncertainty in Arc-Jet Conditions - In all of the work discussed thus far, the operating condition of the facility is assumed to be constant. However, fluctuations in shock-layer emission could be observed visually during the experiments. For one electrode package experiment, the temporal variation of the 7773.4 Å atomic oxygen transition intensity was monitored. A running-averaged signal value was calculated over a fixed time interval. The standard deviation of this averaged signal indicated the fluctuation level of the raw data. For t_{exp} >2 s, the fluctuations became negligible. Thus, in the more recent experiments several neutral density filters were used so that the shutter could be opened longer than 5 s without saturating the CCD camera. This was not done for the axial shock-layer emission surveys, which may help explain the large scatter in T_e values near the shock front for those experiments.[14]

2.5 Summary of Emission Measurements

Results of the analysis of emission signals acquired in the electrode package region indicate that the gas is probably optically thick and that radiative transport must be taken into account. However, by assuming that the flow property and species distributions are uniform across the line-of-sight, a correction for self-absorption was developed and the T_e values derived from O and N emission exhibited good agreement.

Line-of-sight integrated values of T_r, T_v, and T_e were obtained within the shock layer formed over a blunt-body placed in the stream. Profiles were obtained in the axial direction, normal to the blunt-body surface for two different operating conditions and in the radial, or spanwise, direction for the low pressure condition. Simplified interpretations of the emission spectra based on the assumption that the intensity gradients are negligible along the line-of-sight appear to be in error. Results from the radial survey at a single axial location within the shock layer indicate a large region of thermal equilibrium when the temperatures are derived from Abel-inverted intensities. This shock-layer result was obtained at relatively low stagnation pressure with a 15.24 cm diameter flat-faced cylinder. A similar radial survey conducted with the test article out of the stream indicated that the NO γ band emission is relatively uniform over a large spanwise distance. Thus, the rotational temperatures derived from the FWHM of NO-γ bands can be considered to be representative of the stream.

An additional observation from this work is that a ray-trace analysis of the light collection system is required to understand additional degradation of spatial resolution that may result from setting the system f/# too low. This type of analysis can also be used to guide the alignment the system to optimize the distribution of object area dimensions about the target focal location, and thereby minimize off-axis contributions to the light collection. Finally, knowledge of the light collection volume defined by the ray tracing is required in order to reliably compare measured emission spectra with calculations.

Further work will include completing the analysis of the Abel-inverted emission results to assess chemical equilibrium within the shock layer. This analysis is important for determining the state of the shock-layer

flow and may help improve current analytical methods used to relate the arcjet test conditions to flight environments.

3.0 LIF Measurements in Large-Scale Arcjet Facilities

Introduction - The discussion of flow properties derived from emission measurements in large-scale arcjet facilities mentioned two drawbacks to emission-based property measurements: the quantity of measurements required to obtain spatially resolved emission intensities, and the required assumption that the thermodynamic behavior of the sparsely populated excited electronic states is representative of the ground states. Concerns about these issues have motivated investigations of laser-spectroscopic techniques, such as laser-induced fluorescence (LIF). Laser-induced fluorescence techniques offer an attractive alternative to emission-based measurements, because of their ability to probe ground state populations with high spatial resolution. Following a brief introduction to the basic principles of LIF measurements, recent results from applications of LIF to large-scale arcjet facilities are presented and discussed.

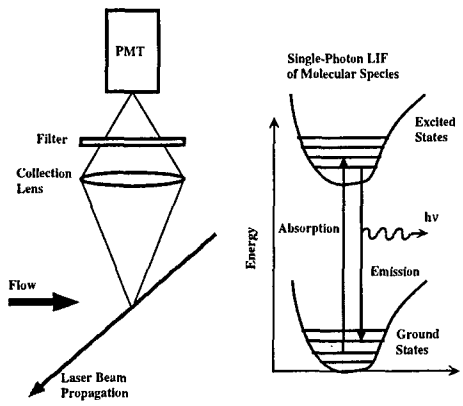

Fig. 30 Single-photon LIF process for a molecular species.

3.1 Laser-Induced Fluorescence

The LIF process involves two steps, absorption and fluorescence. Provided that the allowed absorption transitions for a particular species are optically accessible, then LIF can be used to probe ground state populations. This is important for arcjet flow applications because the ground electronic states of the major species are the most heavily populated. A simplified diagrammatic rendering of LIF is shown in Fig. 30 for a diatomic molecule. At the right of the figure, two bound electronic states with vibrational energy levels are indicated by the potential curves. The LIF process is indicated by the vertical arrows with the upward arrow representing absorption of a photon from the laser and the downward arrow representing fluorescence, which is accompanied by the emission of a photon. Other depopulating mechanisms, such as quenching and predissociation, can also operate on the upper state population.

A generic experimental configuration is shown at the left of Fig. 30 to illustrate the spatially resolved nature of the LIF measurements. Unlike absorption and emission diagnostics, LIF provides localized measurements, since only the volume defined by the intersection of the image of the detection aperture and the laser beam produces the recorded signal. Flow axisymmetry is therefore not required for making spatially resolved LIF measurements. Before discussing how specific flow properties are measured, some background information about the LIF process is required.

Single-Photon LIF Rate Equations - The first step of the LIF process involves the absorption of a photon. Absorption is described by Beer's law,[6] which states that the change in intensity of light at a certain frequency through an optically thin absorbing medium is

$$\frac{dI_\omega}{dz} = -\alpha_\omega \, I_\omega ,$$

which can be integrated directly and rearranged to yield

$$I_\omega = I_{0\omega} e^{-\alpha_\omega z} \quad . \tag{28}$$

Species and thermodynamic information is contained in the absorption coefficient α_ω, which can also be expressed in terms of an absorption cross section[6]

$$\alpha_\omega = n \, f(T) \, \sigma_{12} \phi(\omega) \quad . \tag{29}$$

In the above expression, we have introduced the spectrally integrated cross section σ_{12}, a line shape function $\phi(\omega)$, and shorthand notation for the Boltzmann population fraction $f(T)$.

$$f(T) = \frac{n_i}{n} \frac{g_i e^{-E_i/kT}}{Q} \quad ,$$

which was discussed extensively in the description of emission measurements.

A model of the LIF process is required to determine gasdynamic quantities from measured fluorescence signals. This model can be derived by solving the equations that govern the populations of the energy levels involved in the LIF process. For a simple system consisting of only two, nondegenerate energy levels, the appropriate rate equations are[37]

$$\frac{dn_1}{dt} = -b_{12} n_1 + (b_{21} + A_{21} + Q_{21}) n_2 \tag{30}$$

for the lower level population and

$$\frac{dn_2}{dt} = b_{12} n_1 - (b_{21} + A_{21} + Q_{21}) n_2 \tag{31}$$

for the upper level. In the above equations, n_1 and n_2 are the number densities of the two levels, which

are related through the total population in the initial level before the laser is switched on, $n_1^0 = n_1 + n_2$; b_{12} and b_{21} are the stimulated absorption and stimulated emission rates; A_{21} is the spontaneous emission rate; and Q_{21} is the collisional quenching rate. Predissociation from the upper level is assumed to be negligible. The stimulated absorption rate can be expressed as the product of the spectral absorption cross section, σ_ω, and the photon flux, Φ,[38]

$$b_{12} = \sigma_\omega \Phi \quad , \tag{32}$$

where $\sigma_\omega = \sigma_{12}\phi(\omega)$ and $\Phi = I/\hbar\omega_{12}$.

By using the total population relation to eliminate n_1 from Eq. (31) and integrating directly, the time-dependent expression for the upper state population is obtained,

$$n_2 = \frac{b_{12}n_1^0}{r}\left(1 - e^{-rt}\right) \quad , \tag{33}$$

where $r = (b_{12} + b_{21} + A_{21} + Q_{21})$ is the sum of all the rates. The measured LIF signal depends on the upper state population, and can be expressed in general terms as

$$S(t) = \hbar\omega_{21} n_2(t) A_{21} \frac{\Omega}{4\pi} V_c \quad , \tag{34}$$

where Ω is the solid angle of the collection system that is used to observe the probe volume, V_c, which is defined by the collection optics (often it is the product of the beam area, A_p, times observed length, L).

A pulsed laser system is often employed in arcjet diagnostic applications, and the detection electronics integrate the LIF signal over the laser pulse duration,τ_p. The only time-dependent term in the expression above is the upper state population, so the integral involves

$$\int_0^{\tau_p} n_2(t)dt = \frac{b_{12}n_1^0}{r}\int_0^{\tau_p}\left(1 - e^{-rt}\right)dt \quad .$$

The resulting expression,

$$\int_0^{\tau_p} n_2(t)dt = \frac{b_{12}n_1^0}{r^2}\left(e^{-r\tau_p} - 1\right) + \frac{b_{12}n_1^0\tau_p}{r} \quad ,$$

can be simplified by considering the magnitudes of the rates and the temporal interval. For a pulsed, UV laser system operating near 225 nm, with 0.1 mJ pulse energy, a 1 mm beam diameter at the probe volume and a 10 ns temporal pulse length, the pulse intensity is $\approx 10^6$ W/cm^2. For 225 nm wavelength photons, the photon flux Φ for this intensity is $\approx 10^{24}$ cm^{-2} sec^{-1}. The absorption cross section can be derived from the Einstein A coefficient for spontaneous emission[38]

$$\sigma_\omega = \frac{g_2}{g_1}\frac{\pi^2 c^2}{\omega_{21}^2} A_{21}\phi(\omega) \quad .$$

Using the value published by Eckbreth[37] for A_{21} for the (0,0) band of the NO γ system, and assuming that the combined laser and transition line width has a FWHM of $\approx .3$ cm^{-1} at 225 nm, then $\sigma_\omega(0,0) \approx 5(10)^{-14}$ cm^2. The pumping rate for a NO γ (0,0) transition is then $b_{12} \approx 5(10)^{10}$ sec^{-1} from Eq. (32). This rate dominates all others in the total rate expression, $r = (b_{12} + b_{21} + A_{21} + Q_{21})$, used in this two level analysis. For a typical gate integration time on the order of 100 ns,

$$\left(e^{-r\tau_p} - 1\right) << r\tau_p \quad ,$$

and the following simplified result is obtained,

$$\int_0^{\tau_p} n_2(t)dt \cong \frac{b_{12}n_1^0\tau_p}{r} \quad .$$

With this result, the expression for the temporally integrated energy incident on a photodetector becomes

$$\begin{aligned} S &= \int_0^{\tau_p} S(t)dt \\ &= \hbar\omega_{21}A_{21}\frac{\Omega}{4\pi}V_c n_1^0\tau_p \frac{b_{12}}{(b_{12} + b_{21} + A_{21} + Q_{21})} \end{aligned}$$

By rewriting the total rate expression as

$$b_{12} + b_{21} + A_{21} + Q_{21} = (b_{12} + b_{21})\left(1 + \frac{(A_{21} + Q_{21})}{(b_{12} + b_{21})}\right)$$

and by replacing the stimulated absorption and emission rates with their definitions, (*i.e.*, $b_{12} = B_{12}^\omega I_\omega/c$), the temporally integrated signal can be expressed as,

$$S = \hbar\omega_{21}A_{21}\frac{\Omega}{4\pi}V_c n_1^0\tau_p \frac{B_{12}^\omega}{B_{12}^\omega + B_{21}^\omega}\frac{1}{1 + \frac{I_{sat}}{I_\omega}} \quad ,$$

where $I_{sat} \equiv (A_{21}+Q_{21})c/(B_{12}^\omega+B_{21}^\omega)$ is the saturation intensity[37] and B_{12}^ω, B_{21}^ω are the Einstein coefficients for stimulated absorption and emission. For modest laser intensities, $I_\omega << I_{sat}$, and the expression for the energy incident on the photodetector simplifies further to

$$S = \frac{\Omega}{4\pi}V_c\frac{A_{21}}{A_{21} + Q_{21}} n_1^0(I_\omega\tau_p)\hbar\omega_{21}\frac{B_{12}^\omega}{c} \quad .$$

Finally, if the spectral intensity of the pump laser is defined such that $I_\omega = I\phi(\omega) = \phi(\omega)\int I(t)dt/\tau_p = \phi(\omega)E_p/A_p$, where E_p is the pulse energy, then the detected signal can be written as,

$$S = \frac{\Omega}{4\pi}V_c\frac{A_{21}}{A_{21} + Q_{21}}\frac{E_p}{A_p}\sigma_{12}\phi(\omega)f_1(T)n \quad , \tag{33}$$

where the substitution, $n_1^0 = f_1(T)n$, for the population of the initial level has also been made.

In Eq. (33), the dependence of the LIF signal on thermodynamic parameters is manifested in several terms. The initial population in the pumped level depends on species density, n, and on temperature through the Boltzmann population fraction, $f_1(T)$, while the collisional quenching rate, Q_{21}, depends on the pressure, temperature, and collision partner. Except in rare cases, such as for highly predissociated species or extremely broad laser band widths, the absorption line shape function, $\phi(\omega)$, also depends on temperature and pressure through the mechanisms of Doppler and collisional shift and broadening, which are discussed below for two-photon LIF measurements.

3.2 Single-Photon LIF of Cu and NO

Demonstrations of single photon LIF measurements in arcjet facilities using Cu as the target species have been reported at NASA Johnson Space Center[39,40] (JSC) for pointwise configurations and at ISAS,[41] in Japan, for a planar laser sheet configuration. In the JSC arcjet experiments, the measured LIF signals were analyzed to determine velocity and translational temperature from the Doppler shift and Doppler broadening of the excitation profile at a single location in the arcjet stream.[40] The planar measurements using Cu-LIF at ISAS were used to determine a two-dimensional map of the flow velocity.

Copper is present in most arcjet flows as a result of arc-induced erosion of the copper electrodes, but it is usually (hopefully) a minor species. The two applications of Cu-LIF above indicate the ubiquitous nature of copper in arcjet flows, since the JSC facility is a constricted-arc heater and the ISAS facility used a Huels-type heater. Estimates of copper loading on the order of 100 to 1000 ppm in the test gas flow have been derived from mass loss analyses of electrodes (see Ref. 41, for example) Unfortunately, the copper erosion process is difficult to characterize because electrode erosion is inherently unpredictable. It is likely that copper is introduced into the flow in multiple phases owing to liquefaction of the electrode surface from the intense heating at the arc attachment point. This raises questions about both the spatial and temporal uniformity of the copper distribution in the stream and its fidelity as a tracer atom for velocity measurements.

Nitric oxide has also been used as a fluorescing species in arcjet streams by the same researchers[39,42], as well as the research group at IRS,[43] in Germany. No quantitative measurements of flow properties from NO-LIF were reported from the JSC group, but the other groups used NO-LIF to derive temperature and species information. The enthalpies determined from energy balance methods were typically < 10 MJ/kg for the JSC and ISAS investigations.

For air flows, NO is also a minor species, and depending on the stagnation enthalpy, pressure, and expansion process, concentrations in the free stream vary widely. Results of an investigation of NO LIF in the Ames AHF Arcjet Facility illustrate this point. Based on earlier free-stream emission measurements in the same facility, instrumentation was implemented to probe NO in the free stream flow[44] using LIF to confirm the implied NO (X) populations that were predicted by a computational flow simulation.[27] Despite the sensitivity of LIF for NO (X) population measurements using ro-vibrational transitions of the γ system, no detectable signal was found from the flow centerline. An assessment of the [NO] detectivity of the LIF instrumentation that was used in the investigation[44] indicated that the NO (X) population was $\leq 10^{13}$ cm^{-3}. The absence of a measurable NO (X) population is not surprising, since the enthalpy levels in this facility are typically > 10 MJ/kg. Given that the free stream flow is not in thermochemical equilibrium, the discrepancy between observed NO (A) state emission and absence of NO (X) state absorption is also not surprising. It is possible that the ground state NO population is due entirely to radiative transitions, and therefore may only be on the order of the (A) state population. Alternative mechanisms for producing NO (γ) and (δ) band emission in the free stream are being investigated.

3.3 Two-Photon LIF of O and N

Introduction - Although the single-photon LIF measurements discussed above have yielded useful information about arcjet flows, the two target species most commonly used, NO and Cu, are minor flow constituents. As such, it is impossible to characterize the arcjet test stream from NO or Cu measurements alone. More useful information would be obtained from LIF measurements of the major species, which include atomic oxygen, atomic nitrogen, di-nitrogen, and argon for air flows. For example, it is important to know the degree of dissociation in nonequilibrium arcjet flows, because considerable energy can reside in oxygen and nitrogen chemistry. If the mass flows of the facility gases are known at any point, and atomic species concentrations are measured in the free stream, then the degree of dissociation and chemical energy level can be determined. Unfortunately, single-photon transitions for N and O require an excitation source at VUV wavelengths, which is difficult to implement in large-scale facilities. LIF excitation of O and N is still feasible, however, if two UV photons are used to provide the transition energy.[45]

Two-photon LIF measurements in large-scale arcjet facilities were demonstrated by Bamford and his coworkers in a series of pathfinding investigations conducted in the Ames AHF Arcjet Facility.[46,47] The two-photon

LIF of N technique has been developed further to obtain more information from the flow.[48,49] Results from these more recent investigations are discussed below.

A schematic representation of two-photon LIF is given in Fig. 31, where the excitation process is indicated by the vertical arrows and a single radiative transition from the upper level is shown for both O and N. Note that the experimental configuration is no different from that of single-photon LIF; both single- and two-photon strategies provide spatially-resolved, species-selective information. As was the case for quantitative, single-photon LIF measurements, a mathematical model of the two-photon LIF process for the target species is required to derive gasdynamic flow properties from the measured signals.

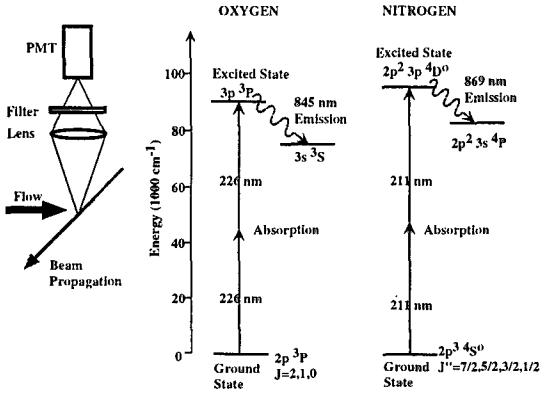

Fig. 31. Two-photon LIF technique and energy levels for O and N that are used in this work.

A complete derivation of the expression for the measured fluorescence signal resulting from two-photon excitation of atomic oxygen is given by Bamford et al.[50] The two-photon nature of the excitation process is manifested primarily in the stimulated absorption rate,

$$b_{12}^{(2)} = \sigma_{\omega}^{(2)} \Phi^2 \quad ,$$

which now depends on the square of the photon flux Φ. In the above expression the two-photon excitation cross section, $\sigma_{\omega}^{(2)}$, is related to the spectrally integrated cross section, $\sigma_{12}^{(2)}$, by

$$\sigma_{\omega}^{(2)} = \sigma_{12}^{(2)} G^{(2)} \phi(\omega) \quad ,$$

where $G^{(2)}$ is the second-order coherence factor that contains the effects of unresolved, ultrafast fluctuations of the laser excitation pulse on the temporally integrated signals.[51]

Using the same UV laser parameters specified in the discussion of rate magnitudes for single-photon LIF above, the stimulated absorption rate can be estimated for two-photon LIF. For the $J = 2$ level of atomic oxygen, the spectral two-photon excitation cross section for line center excitation[50] is $\sigma_{\omega}^{(2)} = 4.8(10)^{-46}$ cm^4 sec. As before the photon flux is $\Phi \approx 10^{24}$ cm^{-2} sec^{-1}, and the stimulated absorption rate is therefore $b_{12}^{(2)} \approx 630$ sec^{-1}. This is roughly eight orders of magnitude lower than the stimulated absorption rate for single-photon excitation of NO, and this rate magnitude disparity illustrates why two-photon LIF strategies are used only when absolutely necessary.

Since the process of deriving the two-photon LIF signal expression is similar to that followed above for the single-photon case, only the result is given here. The expression for the temporally integrated two-photon LIF signal is

$$S = \frac{\Omega}{4\pi} V_c \frac{A_{21}}{A_{21} + Q_{21}} \frac{E_p^2 \int F^2(t) dt}{A_p^2 (\hbar\omega)^2} G^{(2)} \sigma_{\omega}^{(2)} f_1(T) n \quad , \tag{39}$$

where $\int F^2(t) dt$ represents the integral of the square of the laser temporal profile, and the initial population term $f_1(T)n$ accounts for fine level population distributions.

Flow properties derived from LIF signal measurements are usually obtained by comparing, and thereby calibrating, the flow signals with simultaneously measured LIF signals from a reference cell at known thermodynamic conditions.[47–49] For the experiments described below, the reference cell is a flow reactor that uses a microwave discharge to dissociate a fraction of the molecular gas stream at a known pressure and temperature. The beam propagation path is oriented perpendicular to the velocity vector so that the transition line center seen by the reference cell detector is not Doppler-shifted. Signals are acquired from the flow and the reference cell simultaneously by scanning the laser through the transition and recording the measured fluorescence as a function of the scan wavelength.

Following a brief description of the optical configuration for the experiments, discussions of specific methods for measuring velocity, translational temperature, and species density using two-photon LIF of atomic nitrogen are given. Results of flow property measurements, along with estimated experimental uncertainties are then presented for two separate arcjet experiments; one with N_2/Ar flow and the other with air/Ar flow. For each test series, further data analysis is performed to characterize the flow of the free stream based on the LIF measurements. Although LIF measurements have been made in the shock layer,[44] the discussion below will be restricted to free stream measurements. Finally, findings from the stream characterization experiments are summarized.

3.3.1 Experimental Configuration for Free Stream LIF

Although Fig. 31 depicts the elemental components required for making LIF measurements, the actual installation is more complex. The optical configuration for the two-photon LIF experiments in the Ames AHF

Arcjet Facility is shown in Fig. 32. During the arcjet experiments, a frequency-doubled, Nd:YAG-pumped dye laser is scanned through the absorption transition (near 211 nm for N or 226 nm for O) and the resulting fluorescence signal is recorded as a function of wavelength, once the appropriate test conditions have been attained. Approximately 3 minutes are required to scan a single transition, so the measurements represent time-averaged quantities obtained during steady operation of the continuously running arcjet. For the arcjet optical path, the beam is delivered to the test cabin through a series of fused silica prisms and a Galilean telescope. The beam is then transmitted through a fused silica window onto a two-mirror positioner that orients the beam probe volume at an angle relative to the main flow axis. A PMT with a fast preamplifier detects the LIF signals through a side window with f/18 optics and a narrow bandpass filter to reduce background light. For these experiments, LIF measurements were made $\approx$ 15 cm downstream of the nozzle exit, and owing to the 1/6 magnification of the collection optics, the 3 mm aperture restricts the viewed length of the laser beam to 18 mm about the central streamline. Typically, the beam diameter is 1 - 2 mm and only about 150 μJ of laser pulse energy is delivered to the measurement location.

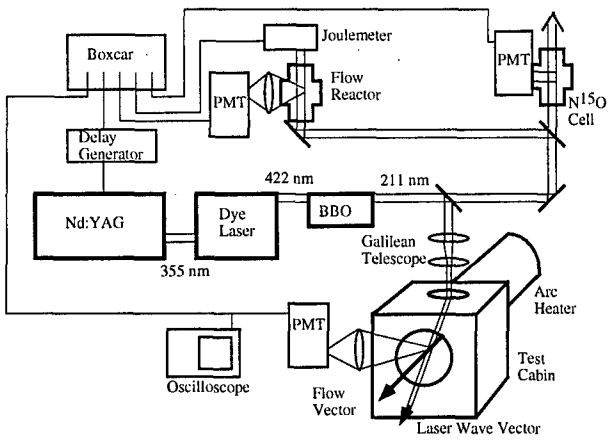

Fig. 32. Optical configuration for the arcjet two-photon LIF experiments.

Two other beam paths are shown on Fig. 32. The first path shows a small portion of the beam being used to excite single-photon LIF in a room temperature, low pressure isotopic nitric oxide, $N^{15}O$, cell. Nitric oxide is a useful wavelength reference molecule in the ultraviolet, and the isotopic form is used in this application to obtain a closer spectral overlap between the $N^{15}O$ and atomic transitions.[44] The second additional beam path in Fig. 32 is directed to the flow reactor, which is used as a temperature and velocity measurement reference, as described above. Fluorescence signals from the cell and reactor are also detected with PMTs. Signals from the laser pulse energy meter and all PMTs are processed by a computer-controlled preamplifier and boxcar unit. Further details on the instrumentation can be found in Ref. 48.

3.3.2 Flow Properties from Two-Photon LIF

Example two-photon LIF signals from atomic nitrogen obtained from the arcjet flow and from the low pressure flow reactor are shown in Fig. 33. The fluorescence signals, which arise from pumping the J= 7/2, $3p^4D^\circ \leftarrow 2p^4S^\circ$ transition of N, are shown as a function of the dye laser fundamental wavelength. The broader, noisier LIF signal was obtained from the arcjet flow and the narrower signal was detected in the flow reactor. Both LIF signals were five-pulse averaged by the data acquisition system. A nonlinear, least-squares fit to the data using a model of the two-photon absorption line shape is also shown for both the reactor and flow signals. The flow reactor conditions given on the figure were measured with a pressure transducer and thermometer at the reactor, while the arcjet flow conditions were determined from the spectra using analytical methods that are described below.

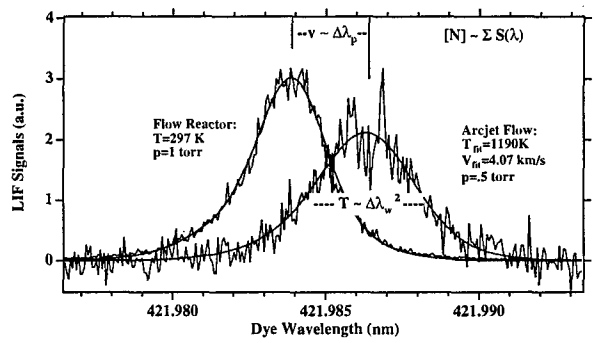

Fig 33. Example spectra from two-photon LIF of N in the flow reactor and the arcjet free stream.

Velocity - In Fig. 33, the central absorption wavelength of the transition for the arcjet flow is shifted relative to the transition location in the flow reactor. This Doppler shift is due to the angular orientation of the beam path relative to the axial flow velocity of the arcjet centerline. Provided that there is no collision-induced shift and the beam angle relative to the velocity vector is known, the gas velocity can be determined from the wavelength shift of the absorption line center using the following relation:

$$v = \frac{c\Delta\lambda}{\lambda \cos\theta}. \qquad (35)$$

In the above expression, v is the flow velocity, c is the speed of light, $\Delta\lambda$ is the difference between the arcjet flow transition wavelength and the unshifted reference wavelength from the flow reactor, and θ is the angle between the light wave vector and the velocity vector.

Translational Temperature - The translational temperature can be inferred from the Doppler width of the excitation line profile. Referring again to Fig. 33, the spectral width of the transition measured in the arcjet flow is considerably broader than that measured

in the flow reactor, which indicates that the arcjet flow temperature is greater than the reactor flow temperature. Generally, multiple broadening mechanisms contribute to the total spectral width of the excitation line profile. For the arcjet and flow reactor test conditions however, the profile is dominated by the combined effect of the laser line width and Doppler broadening. The Doppler broadening contribution for an unknown flow temperature can be deconvolved from the total transition line width by determining the laser line width from an excitation profile measured at a known temperature. Once the transition line widths have been derived from spectral fits to the line shapes, the translational temperature is obtained from the following relation

$$T = \frac{M_N c^2}{8ln(2)kn_A\hat{\nu}^2}\left[\Delta\hat{\nu}^2_{T,F} - (\Delta\hat{\nu}^2_{T,R} - \Delta\hat{\nu}^2_{D,R})\right], \quad (36)$$

where M_N is the molecular weight of N, k is Boltzmann's constant, n_A is Avogadro's number, $\hat{\nu}$ is the transition central wavenumber in cm^{-1}, the $\Delta\hat{\nu}_{I,J}$ are the relevant line width values (FWHM), and the subscripts identify the widths as either Flow, Reactor, Total, or Doppler.

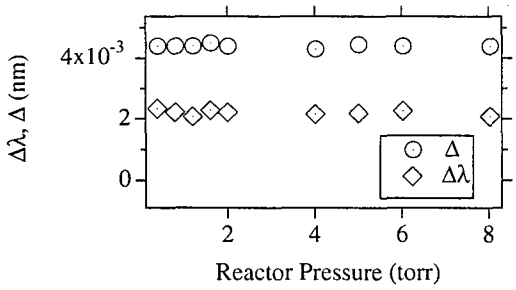

Fig. 34. Measured transition spacing, Δ, and width, $\Delta\lambda$, in the N/N_2 flow reactor as a function of the cell pressure. Note that there is no increase in either parameter with increasing pressure.

Collisional Effects - Since velocity and translational temperature are determined from spectral fits to the measured two-photon excitation line shape, the influence of collisional effects was investigated by recording the excitation line shape in the room temperature, N/N_2-flow reactor at various pressures. The excitation line shapes were then fit with the spectral model, and the location and width of the N atom transition were determined from the fit. The transition location was measured relative to the wavelength of the P_1 (6) rotational transition of the $N^{15}O$-β (2←0) vibrational band. Results from these tests are shown in Fig. 34, where the relative N atom transition location, Δ (nm), and transition width, $\Delta\lambda$ (nm), are shown as function of cell pressure. Neither the location or the width change significantly as the pressure is varied from 0.4 to 8 torr at room temperature. If the dominant collisional mechanism arises from dispersion forces, then the collisional broadening and shift should scale thermodynamically as $pT^{-.7}$.[52] Thus, for typical conditions within the arcjet free stream where $pT^{-.7} << 8(293)^{-.7}$ (torr/$K^{.7}$), collisional processes should have negligible influence on the excitation line shape.

Species Concentration - The spectrally integrated LIF signal is proportional to the concentration of the absorbing species in the laser probe volume. In previous publications of AHF arcjet LIF measurements, the N atom concentrations were presented as relative values, because there had been no measurement of the absolute two-photon excitation cross section for the transition.[47] In a series of recent experiments, both the excitation cross section for this transition, $\sigma^{(2)}_{12}$, and the second order coherence factor, $G^{(2)}$, for the laser used in these experiments have been measured. A preliminary value of the spectrally integrated $\sigma^{(2)}_{12}G^{(2)}$ product for the J= 7/2, $3p^4D^\circ$ ←$2p^4S^\circ$ transition of N in the favorable detection orientation $(2.81(10)^{-35}$ cm^4-rad) is used in this work to convert relative N atom concentration measurements to absolute values. The orientation of the detection optics must be considered because the N atom fluorescence is polarized.[53]

Additional measurements that quantify the pump laser characteristics, light detection efficiency, and upper state lifetime are required to convert the spectrally integrated fluorescence signals to absolute species concentrations. The upper state lifetime, τ_{obs} is used to account for collisional quenching of the fluorescence signal, and it is measured during the excitation scan using a fast digital oscilloscope. Other parameters, including the laser pulse energy in the cabin, E_P, its spatial distribution, A_P, and the laser pulse temporal profile, $\int F^2(t)dt$, were measured daily. Finally, the detection system calibration factor, D, was measured in a Raman scattering experiment (in the manner described in Ref. 54) once the flow measurements were completed. With these additional measurements, the absolute N density can be obtained by rearranging the rate equation solution for two-photon excitation given in Eq. (34) above,

$$n_N = \frac{4\pi}{D}\frac{\tau_{rad}}{\tau_{obs}}\frac{A_P}{\int F^2(t)dt}\frac{(h\nu)^2}{G^{(2)}\sigma^{(2)}_{12}}\int\frac{S_N}{E_p^2}(\omega)d\omega, \quad (37)$$

where τ_{rad} is the radiative lifetime $(43 \pm 3$ ns)[55] of the transition, and S_N is the LIF signal in V.

3.3.3 Two-Photon LIF Measurements in N_2/Argon Flows

Test Conditions - Two-photon, N atom LIF measurements were conducted during three different facility runs at two different heater pressures for N_2/Ar flows. The two different pressures were nominally 2.4 and 4.8 atm, and the currents were varied from about

1200 A at the lower pressure to about 2200 A at the higher pressure. An attempt was made to acquire measurements at four different arc current values during a single facility run at each of the two heater pressures. However, at the lower pressure two separate runs were required to obtain the measurements owing to operational instability of the steam vacuum system during extremely hot weather. Geometrically, the arcjet was configured with a 6 cm diameter heater, a 3.8 cm diameter throat, and a 30.5 cm nozzle exit diameter, which gave an area expansion ratio of 64. Facility operating conditions for these tests are summarized in Table II, and the uncertainty in the parameters is currently estimated to be $\approx$ 5% of the listed value.

Table II. Arcjet test conditions for LIF experiments in N_2/Ar flow.

Arcjet Run Conditions			
Run	Pressure	Current	Voltage
	atm	A	V
21	2.44	1165	3732
	2.50	1388	3565
22	2.35	1563	3263
	2.39	1771	3165
23	4.78	1556	5626
	4.86	1782	5408
	4.73	1964	4981
	4.80	2197	4826

For each measurement, the arc current was adjusted and a scan was taken when the facility condition stabilized. Once the spectral scan was acquired for a current setting, the next condition was set. Flow property measurements from these tests are presented below as functions of the arcjet control variables, pressure and arc current. Uncertainty estimates for each flow property measurement were obtained using the approach outlined in the introduction along with the expressions derived above that relate the properties to the measured signals.

Velocity Measurements - Velocities measured in the free stream of the arcjet flow at each operating condition are shown in Fig. 35. Measured values were obtained from the excitation spectra using Eq. (35). On the figure, the velocities are shown as a function of the arc current, and the circular symbols represent measurements at the 2.4 atm heater pressure, while the diamond symbols represent 4.8 atm pressure values. The measured velocities range from about 3.8 to 4.8 km/s, and two interesting trends are apparent in the data. First, for a given heater pressure, there does not appear to be a significant increase in the stream velocity as the arc current is increased. Second, when pressure is increased, flow velocity appears to increase. Currently, the estimated uncertainty in the velocities is about 6% of the measured value, owing mainly to the uncertainty in determining the difference between the Doppler-shifted and unshifted wavelengths from the spectral fits to the data.

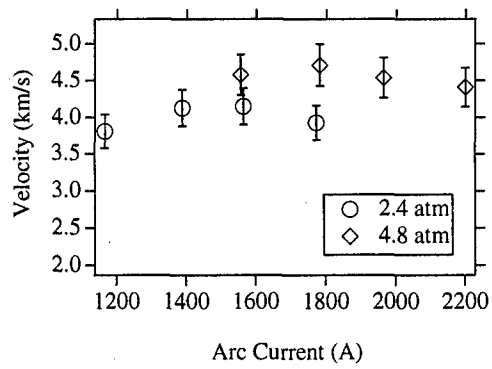

Fig. 35. Arcjet free stream velocities as a function of arc current at two different heater pressures.

Translational Temperature Measurements - Translational temperatures obtained from the measured spectral width of the two-photon transition of N are presented in Fig. 36. The measured values were derived using Eq. (36), and are shown as a function of the arc current for the two different heater pressures. As before, the circles denote the 2.4 atm values and the diamonds represent the 4.8 atm measurements. Measured translational temperatures range from about 800 to 1800 K. Given the estimated uncertainty level, which is 25% of the measured value, it is difficult to distinguish trends for temperature as a function of arc current. Generally, the temperatures at the higher pressure are greater than those at the lower pressure, which would be consistent with the greater sound speed indicated by the velocity measurements (assuming the local Mach number does not change significantly with pressure). The ability to accurately determine the spectral widths of somewhat noisy LIF signals is again the leading contribution to the uncertainty.

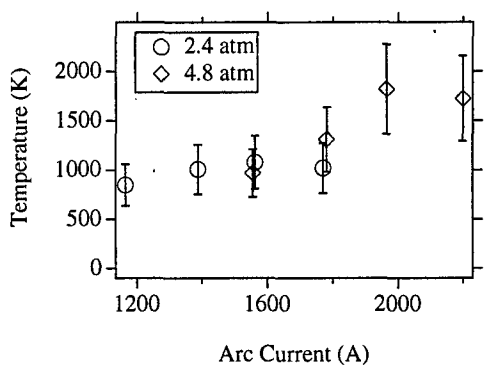

Fig. 36. Measured translational temperatures in the arcjet free stream as a function of arc current.

Table III. Beam and collection parameters for [N] measurements.

Parameter	Value	Units
$G^{(2)}\,\sigma^{(2)}$	$2.81(10)^{-35}$	$cm^4 rad$
D	$1.93(10)^{-8}$	V-cm-sr
A_p	.029	cm^2
$\int F^2(t)dt$	$1.91(10)^{8}$	s^{-1}
$h\nu$	$9.415(10)^{-19}$	J

N Concentrations - Absolute and relative N atom number density measurements are shown in Fig. 37 for the variable current, constant pressure arcjet tests. The absolute [N] values (circles and diamonds) are shown as a function of arc current, while the relative values (squares and triangles) are shown at currents that are shifted by 40 A for clarity. The measured absolute [N] values were obtained from the spectrally integrated, free-stream LIF signals using Eq. (37). Values of the laser pulse spatial and temporal characteristics, the detection calibration constant, and other parameters used to convert the integrated signals from these measurements to absolute N concentrations are given in Table III. Observed fluorescence lifetimes that were recorded during the measurements at each condition are given in Table IV. Measured values of [N] range from $4(10)^{15}$ to $11(10)^{15}$ cm^{-3}. Currently, the uncertainty in the [N] measurements is estimated to be about 28%. Nearly all of this uncertainty is introduced in the conversion of relative to absolute values, with the uncertainty in $G^{(2)}\sigma^{(2)} \approx 25\%$ as the leading contributor. In contrast, the uncertainty in the relative [N] values is only about 5% of the measured value; therefore, trends in the measurements can be inferred from the variation in the relative values. For both the low pressure (squares) and high pressure (triangles) cases, there appears to be a trend of increasing [N] with arc current. At the higher pressure, for which the total mass flow has also increased, the [N] values are all consistently greater than the values for the lower pressure case.

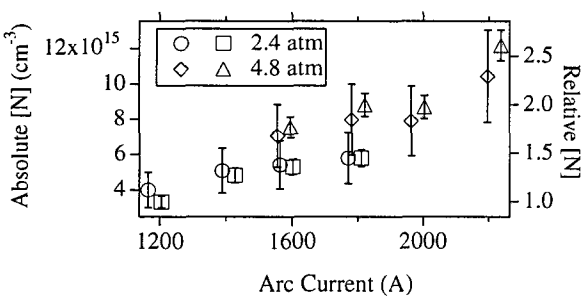

Fig. 37. Absolute and relative [N] as a function of arc current. The relative values, denoted by the squares and triangles, are shifted by 40 A from the absolute values.

For the two flow properties measured with the lowest uncertainty, v and relative [N], trends in the data may provide information about the chemical freezing process that occurs in the nozzle. As current is increased at constant pressure, [N] increases in the free stream, which may indicate that changing the arc current at these conditions does not change the point at which [N] freezes. Energy added to the flow by increasing the discharge current increases N_2 dissociation rather than increasing the kinetic energy of the stream. When pressure is increased, v increases, which may indicate that the [N] freeze point in the nozzle changes due to the increased collisional frequency at the higher pressure. This change in the chemical freezing location may provide more kinetic energy to the flow. Although [N] clearly increases with increasing pressure, some of this increase can be attributed to the increased stream density. With additional information from facility instrumentation, these LIF-based measurements can provide further information about the thermochemical state of the free stream.

Table IV. Fluorescence lifetimes, pitot pressures, and mass flow rates for the arcjet tests.

Lifetimes & Facility Measurements				
Run	τ_{obs}	p_p	$\dot{m}_T$	$\dot{m}_{Ar}$
	ns	torr	kg/s	kg/s
21	36.2	40.4	0.10	0.03
	33.8	41.2	0.10	0.03
22	33.3	39.7	0.11	0.03
	34.7	40.1	0.11	0.03
23	33.7	69.0	0.19	0.03
	34.5	70.0	0.19	0.03
	36.3	68.0	0.20	0.03
	37.0	67.9	0.20	0.03

Stream Characterization - To calculate N mass fractions and other flow properties from the LIF-determined stream properties requires additional information from facility measurements of mass flow and pitot pressure. These quantities are summarized in Table IV for each run and the uncertainties are currently estimated to be between 5 and 10% of the values given. The total mass flow rate, $\dot{m}_T$, and the argon mass flow rate, $\dot{m}_{Ar}$, were determined from the manifold pressures based on earlier facility tests.[56] Also, a flat-faced cylinder with a pressure tap was placed in the test stream to measure the impact, or pitot pressure behind the shock. By rearranging the supersonic Rayleigh formula for pitot pressure[57] and making use of the LIF measurement of velocity, the total stream density, ρ, can be obtained,

$$\rho = \frac{p_p}{v^2}\gamma\left(\frac{2\gamma}{\gamma+1}\right)^{\frac{1}{\gamma-1}}\left(\frac{\gamma+1}{2}\right)^{\frac{-\gamma}{\gamma-1}}, \quad \text{for} \quad M >> 1. \tag{38}$$

Note that density is only a weak function of γ, and that γ only changes by about 30% going from a molecular to completely dissociated gas. Thus from the measured pitot pressure, velocity, and an estimate of γ (≈ 1.45)

the stream density can be calculated. This allows a determination of the N mass fraction, w_N, from

$$w_N = \frac{n_N M_N}{\rho n_A}. \quad (39)$$

Assuming that the ion and excited electronic level populations are negligible, the mass fractions of the remaining flow constituents can be determined from

$$w_{Ar} = \frac{\dot{m}_{Ar}}{\dot{m}_T}, \quad (40)$$

and

$$w_{N_2} = 1 - w_{Ar} - w_N.$$

Using the constituent mass fractions, a closer estimate of γ can be developed by iterating between Eq. (38) and the above relations, although there is no information on N_2 vibration, as discussed below.

Table V. Constituent specific heats, gas constants and molar masses used in Eqs. (39),(41), and (42).

N_2/Ar Flow Species Thermodynamic Properties			
Species	c_{pi}	R_i	M_i
	MJ/kg-K	MJ/kg-K	kg/mol
Ar	$2.5R_{Ar}$	208	.040
N	$2.5R_N$	594	.014
N_2	$4.5R_{N_2}$	297	.028
O	$2.5R_O$	519.6	.016

Assuming that N_2 vibration is fully excited, the total flow enthalpy can then be calculated from the measured values of velocity, translational temperature, and the derived mass fractions,

$$h_T = \sum_i w_i c_{pi} T + \frac{v^2}{2} + w_N R_{N_2} \Theta_{dN}, \quad (41)$$

where c_p is the specific heat and Θ_{dN} is the characteristic dissociation temperature of N (113,000 K, Ref. 58). As will be shown below, the contribution of the thermal mode, which includes vibrational energy, to the total flow enthalpy is quite small. Note that the free stream LIF-based approach to determining the enthalpy provides the apportionment among the chemical, thermal, and kinetic modes directly.

Using the above relations and values for the constants that are given in Table V, values of the mass fractions and total enthalpies were determined for the arcjet tests. The N mass fractions are shown in Fig. 38 as a function of arc current for the tests at the two different heater pressures. Now the effect of the increased stream density at the higher chamber pressure is more apparent, and w_N may actually decrease as pressure is increased at constant current. This would support the earlier suggestion of increased N recombination arising from the greater collision frequency at higher chamber pressure. Note that the degree of N dissociation, $\alpha_N = w_N/(w_N + w_{N_2})$,[58] on the free stream centerline is substantial, ranging from .33 to .56 for these test conditions.

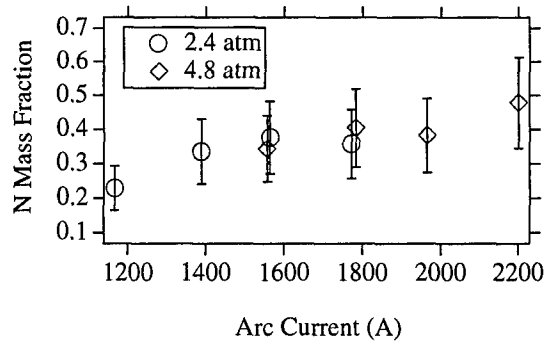

Fig. 38. Atomic nitrogen mass fraction as a function of arc current in the arcjet free stream.

The total flow enthalpies determined from the measured flow properties using Eq. (41) are given in Fig. 39. Values range from 16 ± 3 MJ/kg at the lowest current of the low pressure test to 28 ± 6 MJ/kg at the highest current of the high pressure test case. For both values of the heater pressure, the total enthalpy appears to increase with increasing arc current, as expected.

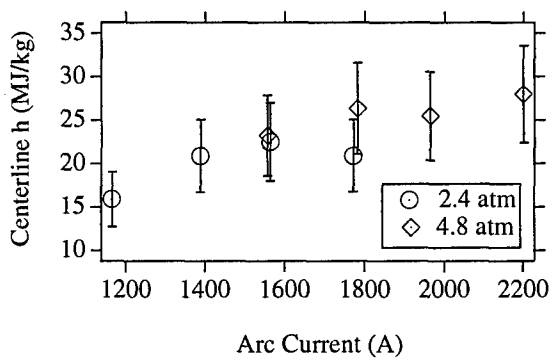

Fig. 39. Total enthalpy on the arcjet free stream centerline as a function of the arc current.

The fractional contributions of the separate modes to the total enthalpy are plotted in Fig. 40. For these test conditions, the dominant contributions to the total enthalpy come from the N_2 dissociation, or chemical mode, and the kinetic mode. The total thermal contribution to the free stream flow enthalpy is always less than 10% . This suggests that even a fully-excited N_2 vibrational contribution (with $T_v = 2T_{tr}$) to the total enthalpy would be less than 1%, so the penalty for the assumption of full excitation in the preceding analysis appears to be small. This plot also shows which flow properties need to be measured most accurately, v and [N], to improve the precision of the enthalpy determination.

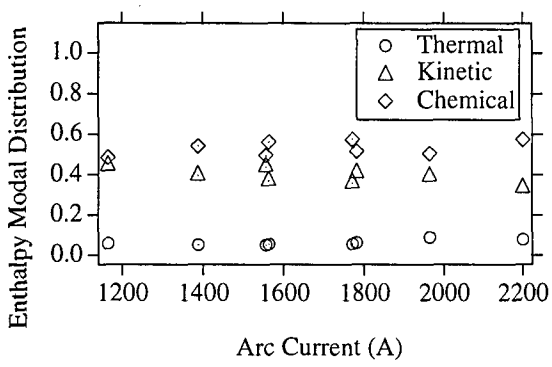

Fig. 40. Fractional distribution of the total centerline enthalpy as a function of the arc current.

Additional properties that were determined for the tests are the flow Mach number, $M = v/\sqrt{\gamma RT}$, which ranged from 4.2 to 6.2, and the static pressure, $p_s = \rho RT$, which varied from 0.9 to 2.8 torr.

3.3.4 Two-Photon LIF Measurements in Air/Argon Flows

Flow property and stream characterization measurements obtained using two-photon LIF of N have also been performed for air/Ar test gas flows in the same arcjet facility. Results from these experiments are discussed below.

Test Conditions - Two sets of LIF measurements in air/argon gas mixtures were obtained for variable current settings at two different nominal constrictor pressures, 2.4 and 4.8 atm. An additional set of measurements was acquired at the lower pressure. For all three runs, the geometric configuration of the arcjet facility was identical to that mentioned earlier for the N_2/Ar tests. Facility operating conditions for the three tests are summarized in Table VI.

Table VI. Test conditions in the AHF Arcjet for the variable current, constant pressure LIF experiments in air/Ar flows.

Arcjet Run Conditions			
Run	Pressure	Current	Voltage
	atm	A	V
11	2.44	1149	3198
	2.51	1333	3115
	2.58	1556	3067
15	2.43	1130	3218
	2.37	1357	2991
	2.43	1545	2926
	2.46	1761	2855
19	4.78	1836	4454
	4.86	2016	4309
	4.80	2237	4206

For the results reported below, the uncertainties in the measured flow properties are greater than those for the N_2/Ar flow results owing to the reduced signal levels that resulted from dilution of the N population by atomic oxygen.

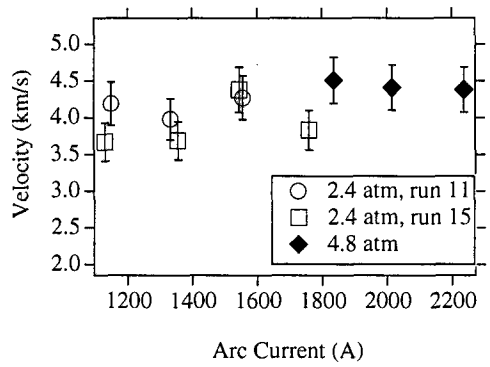

Fig. 41. Arcjet free stream velocities as a function of arc current at two different heater pressures.

Velocity Measurements - Velocity measurements as a function of arc current are shown in Fig. 41 for the three runs at constant pressure. The lower pressure (2.4 atm nominal) results from two different runs are denoted by the open circles and squares, while the results from the higher pressure run are represented by the solid diamonds. Uncertainties for the velocity measurements are about ± 7%, and measurements from the two lower pressure runs agree to within this amount. The lower pressure data appear to indicate increasing velocity with increasing current for each run, while the higher pressure measurements appear to indicate the opposite trend. This suggests that the arc current has little effect on flow velocity. However, all of the velocities from the higher pressure run are greater than for the lower pressure cases. Both observations are consistent with trends noted in previous experiments.[48,49]

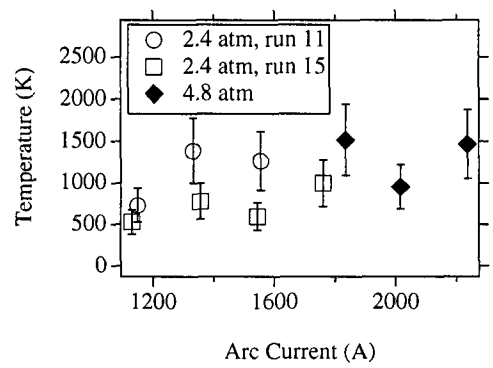

Fig. 42. Measured translational temperatures in the arcjet free stream as a function of arc current.

Translational Temperature Measurements - Measured flow translational temperatures that were derived from the N atom transition line width are shown in Fig. 42, using the same symbol convention to denote the separate runs. Owing to the high uncertainty, which is 30 % of the measured value, it is difficult to discern trends in translational temperature with increasing arc current, although the mean value

of measured translational temperature is higher for the higher pressure, higher current conditions than for the lower conditions. Measured values from the two lower pressure tests generally agree to within their estimated uncertainty.

N Concentration Measurements - In contrast to the velocity and translational temperature, consistent trends of increasing relative N atom concentration with increasing arc current were observed for both lower pressure and higher pressure tests, as shown in Fig. 43. Relative N concentrations that are normalized to the value measured at the lowest current are shown as a function of arc current. Because [N] is determined from the spectral integration of the absorption line shape, the lower N atom LIF signal for air/argon flows has less of an impact on the concentration measurements. The low pressure test results show a lower rate of increase in relative concentration with increasing current than the 4.8 atm results. At the lowest current of the high pressure test case, the relative [N] is lower than that of the highest current of the lower pressure test. This may be attributed to increased recombination in the nozzle resulting from the higher pressure.

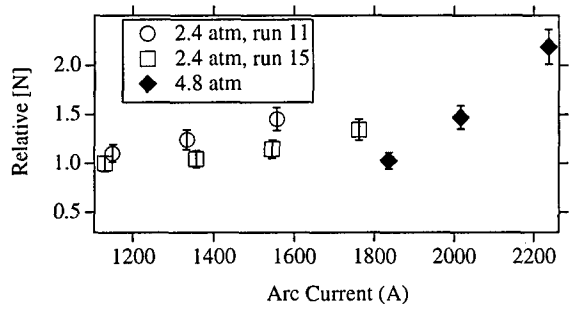

Fig. 43. Relative [N] as a function of arc current.

Absolute N concentrations are plotted as a function of arc current in Fig. 44 using symbol conventions that are consistent with the preceding figures. Upper state observed lifetime measurements, which are required to account for collisional quenching in calculating the [N] values, are given in Table VII. For these experiments, only a limited number of lifetime measurements were made, so mean lifetime values were calculated for the lower and higher pressure cases and applied to all the measurements. As noted in earlier work,[48] the observed lifetimes indicate that collisional quenching is relatively weak at these test conditions. Uncertainty in the product of the two-photon absorption cross section and the second order coherence factor for the laser was again the leading contributor to the total uncertainty in the absolute N concentration measurements. Currently, the uncertainty in these absolute [N] measurements is estimated to be about 30 %, which is considerably greater than the uncertainty in the relative [N] values. Despite the relatively large uncertainty, the absolute concentration values are a critical component of the further analysis of the thermochemical state of the flow.

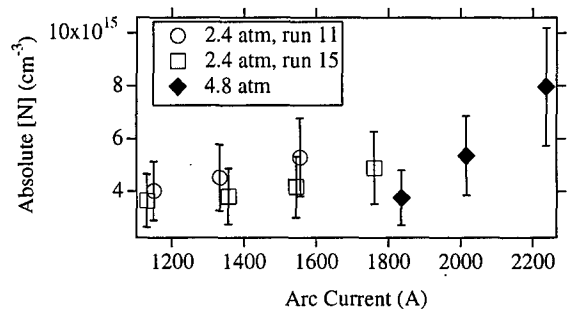

Fig. 44. Absolute [N] as a function of arc current.

Stream Characterization - With the aid of certain assumptions, it is possible to make an assessment of the total stream enthalpy on the flow centerline using the LIF measurement results. The approach is similar to that outlined above for N_2/Ar flow experiments. However, the expression for the free stream enthalpy given by Eq. (41) must be modified to account for the presence of atomic oxygen,

$$h = v^2/2 + w_N R_{N_2} \Theta_{dN} + w_O R_{O_2} \Theta_{dO} + \sum w_i c_{p_i} T. \quad (42)$$

This expression again represents the sum of the contributions of the different modes; kinetic, chemical, and thermal; to the total enthalpy. The characteristic dissociation temperature used in the above expression is $\Theta_{dO} = 59{,}500$ from Ref. 57. As with N_2/argon flows, the velocity and translational temperature are obtained directly from the LIF measurements, while the mass fractions require input from additional facility measurements. Values of total mass flow and argon mass flow that were derived from manifold pressures for the current tests are given in Table VII, along with pitot pressure measurements.

Table VII. Fluorescence lifetimes, pitot pressures, and mass flow rates for the air/argon flow tests.

Lifetimes & Facility Measurements				
Run	τ_{obs}	p_p	$\dot{m}_T$	$\dot{m}_{Ar}$
	ns	torr	kg/s	kg/s
11	35.0	40.4	0.110	0.030
	35.0	42.3	0.110	0.030
	35.0	44.1	0.110	0.030
15	35.0	42.6	0.105	0.030
	35.0	42.1	0.105	0.030
	35.0	42.5	0.105	0.030
	35.0	42.6	0.105	0.030
19	33.1	70.7	0.200	0.030
	33.1	70.1	0.200	0.030
	33.1	69.8	0.200	0.030

The argon mass fraction values for these tests were determined from the ratio of measured argon mass flow to the total mass flow. For all of the tests conducted

to date there has been no evidence to suggest that any oxygen-bearing molecular species are present in the stream. Therefore, the assumption is made that oxygen is completely dissociated, $w_{O_2} = 0$, which allows the O atom mass fraction to be determined from the total mass flow,

$$w_O = .21(M_{O_2}/M_{air})(1 - w_{Ar}), \qquad (43)$$

where M_i are the species molar masses. A further discussion of oxygen dissociation is given below.

Atomic nitrogen mass fraction values were determined using the same method presented above for N_2/Ar flows, which involved determining the stream density from the pitot pressure measurements using Eq. (38) and then using the stream density and [N] measurements in Eq. (39). The N_2 mass fraction is then calculated from

$$w_{N_2} = 1 - w_{Ar} - w_N - w_O.$$

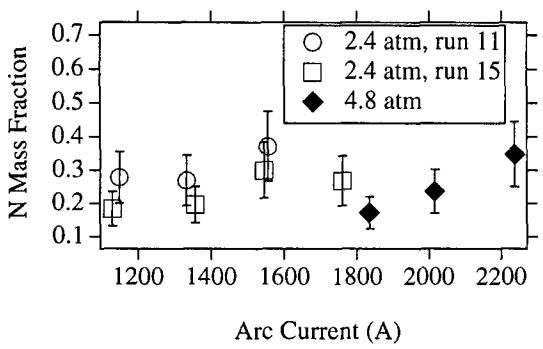

Fig. 45. Nitrogen atomic mass fraction as a function of arc current in the arcjet free stream.

Atomic nitrogen mass fractions derived from the absolute [N] and velocity measurements are shown in Fig. 45 for the three air/Ar runs. Trends for each of the runs are similar to those described in the [N] measurements. However, the effect of the increased stream density at the higher chamber pressure is more apparent, and w_N may actually decrease as pressure is increased at (nearly) constant current. This is consistent with the idea of increased N recombination arising from the greater collision frequency at higher nozzle pressure. Note that the degree of N dissociation, α_N, on the free stream centerline is again substantial, ranging from .26 to .62 for these test conditions.

As with the N_2/Ar flow case, there is no information about the vibrational state of N_2 in the nonequilibrium air/Ar flow. However, the same assumption is made here that the N_2 vibrational energy mode is fully excited, which gives the maximum possible specific heat for N_2.

Total centerline flow enthalpies near the nozzle exit were determined from the measured flow properties using Eq. (42) and the constants given in Table VIII. The results are shown in Fig. 46. Values range from 16 MJ/kg at the lowest current of the low pressure test to 26 MJ/kg at the highest current of the high pressure test case. As with the N_2/Ar results, the total enthalpy appears to increase with increasing arc current. Uncertainties in the total enthalpies are currently estimated to be about ± 30 % of the derived values, based on the propagation of the primary variable uncertainties through Eq. (42). Since the uncertainty contributions from the measured parameters are weighted by their fractional contribution to the total enthalpy, the leading contributors to the uncertainty are the velocity and absolute nitrogen concentration.

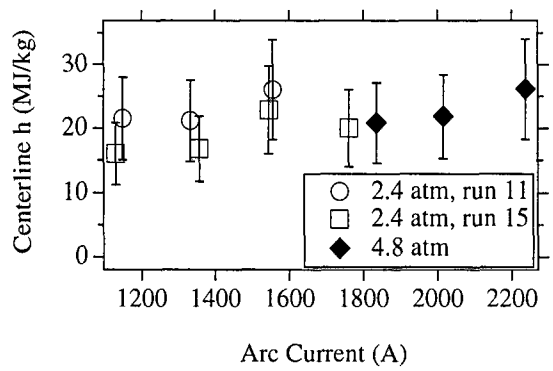

Fig. 46. Total enthalpy on the arcjet free stream centerline as a function of the arc current.

For these air/Ar flow test conditions, the dominant contributions to the total enthalpy come from the N_2 dissociation ($w_N R_{N_2} \Theta_{dN}$), and the kinetic energy ($v^2/2$). The total thermal contribution ($\sum w_i c_{p_i} T$) to the free stream flow enthalpy is again less than 10% at all of the test conditions. This suggests that the vibrational contribution is also negligible for air/Ar flows at these conditions.

Oxygen Dissociation Level - The recent LIF measurements have been directed toward developing and demonstrating the ability to measure enthalpy in the free stream using two-photon excitation of N.[48,49] To use this approach for air/Ar flow mixtures, oxygen is assumed to be fully dissociated. Based on the results of the [N] measurements and the derived dissociation levels, the amount of nitrogen dissociation is substantial ($\alpha_N = .26 - .62$). Since it is energetically easier to dissociate oxygen, the degree of oxygen dissociation should be greater than that of nitrogen.

Additional information on the state of oxygen in the arcjet free stream can be found from the results of experiments undertaken to assess NO populations.[44] During those tests, no laser-induced emission was detected from either the NO-γ system or the O_2 Schumann-Runge bands, which both have a large number of ro-vibrational transitions near 226 nm.[59] Based on their single-photon LIF detectability, a conservative

estimate of approximately 10^{13} cm^{-3} can be placed on the upper population limits for NO and O_2.

From these observations, it was expected that all of the oxygen population would appear as ground state (^{3}P) atomic oxygen. Thus, a comparison between the absolute [O] measurements from the earlier LIF experiments of Ref. 47 and values calculated from the facility mass flow correlations should support this premise. These [O] measurements were carried out by measuring the total LIF signal of a single fine-level transition (J"=2) and using the Doppler width based temperature measurement to account for the fractional population residing in the other fine levels of the ^{3}P ground state. Results from the measurements are shown in Fig. 47, along with calculated population levels derived from the facility mass flow correlations (Eq. (38), above). Both measured and calculated [O] values are shown as a function of chamber pressure, to be consistent with the original presentation of the data.[47] At all but the lowest pressure conditions, the LIF measurements indicate a lower [O] value than expected from the facility data.

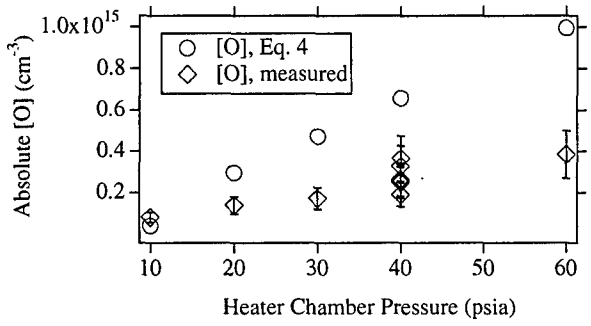

Fig. 47. Comparison of measured and calculated [O] as a function of the heater pressure for tests in the 61 cm diameter nozzle. (Note that Eq. (4) refers to Eq. (38).)

Assuming that the facility correlations are reliable, it is possible that the total O atom population may be under-measured by the LIF approach owing to populations in the two low-lying, metastable singlet states, ^{1}D and ^{1}S. Since these two states do not have an allowed optical transition path to the ^{3}P state, populations can build up as a result of optical transitions from higher electronic levels and remain trapped due to the essentially collisionless free stream environment. Significant metastable state populations would not affect the assumption of full O_2 dissociation, but would affect the overall energy balance since the amount of energy carried by the O atoms is greater for the ^{1}D and ^{1}S levels. If all of the [O] difference is assumed to lie in the highest energy state, then the centerline enthalpy values calculated using Eq. (42) would increase by up to 6 %. While this amount is within the current uncertainty of the centerline enthalpy values, the possibility of O atom metastable state populations should be investigated further.

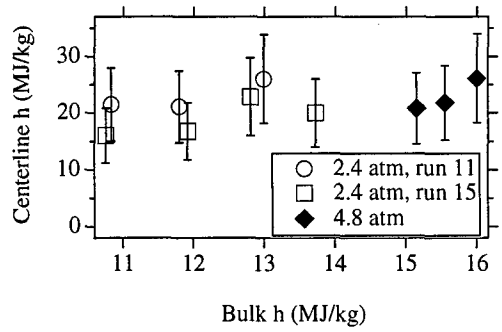

Fig. 48. Measured centerline enthalpies as a function of calculated bulk enthalpies for the air/Ar flows.

Comparison with Bulk Enthalpy - Although the efficiency of the constricted arc heater has not been measured recently for the AHF, measured values obtained from a similar constricted arc heater were used to estimate the bulk flow enthalpy, using the following relation,

$$h_B = \frac{\eta_H V I}{\dot{m}_T} \tag{44}$$

Figure 48 shows the LIF-measured centerline enthalpies as a function of the bulk enthalpy values calculated from the facility correlations for the three different constant pressure, variable current test cases. For each test, the measured centerline enthalpy value appears to increase with increasing bulk enthalpy. The change in measured centerline enthalpy from the lowest current, lowest pressure condition to the highest current, highest pressure condition is 62 %, while the change in bulk enthalpy calculated over these same conditions was 60 %. While this agreement in the relative enthalpy change is noteworthy, the measured enthalpy values on the flow centerline are typically 30 to 50 % greater than the corresponding bulk enthalpy values. This may indicate a nonuniform enthalpy distribution in the stream, but further confirmation by off-centerline measurements is required.

3.4 Summary of LIF Results

The stream information derived from the LIF experiments illustrates the advantage of making spatially resolved measurements using a major flow species. For arcjet flows in particular, probing the most energetic dissociation product allows a determination of the chemical energy in the stream. Moreover, in combination with the species concentration, the additional LIF-based flow property measurements yield a measure of the stream enthalpy and the distribution of energy among the kinetic, chemical, and thermal modes. A measurement of the total enthalpy alone is important, because credible flow simulations and analyses are not possible without it. By knowing the distribution of energy and the flow mass fractions, the degree of nonequilibrium of the free stream in an arcjet flow

can be largely quantified, although there is as yet no information on the vibrational temperature.

From the analysis of the LIF measurements obtained in the Ames AHF Arcjet Facility, it appears that there is more stream energy in the kinetic and chemical modes that in the thermal mode. When the current is increased at nearly constant pressure, only the N concentration appears to change significantly. Comparisons between measured and calculated O concentrations indicate that the flow may be even more energetic than the N LIF measurements imply, since some of the metastable, singlet states of O may be populated in high-enthalpy air flows.

Future work with the LIF instrumentation will be directed toward assessing the magnitude of possible flow property gradients in the radial direction in the free stream. In addition, excitation strategies are being developed to attempt to quantify possible metastable state populations and vibrational temperatures.

4. Summary of Arcjet Characterization Using Optical Diagnostics

Recall that one of goals of these lectures was to argue a case for aerothermodynamic testing in arcjet facilities. In this context, the term aerothermodynamic refers to testing that involves more than simply measuring the thermal response of a material to a measured, but not necessarily known heat flux. Where does this argument stand in light of results from recent experiments performed using optical diagnostics? First, the results from the 2-photon LIF measurements indicate that characterization of the arcjet free stream is feasible. However, further measurements are required to establish the appropriateness of assumptions invoked in the use of the measured quantities and the validity of the approach. Although it is only a limited validation, some insight may be gained by comparing enthalpies derived from the free stream LIF measurements with enthalpies derived from electrode package emission measurements. Each approach relies on different assumptions to determine enthalpy, so the comparison can be useful, and this is currently being investigated.[25]

The second issue involved in using arcjet facilities for aerothermodynamic simulation concerns the state of the gas within the shock layer. In arcjet flows, a highly dissociated free stream gas passes through a relatively weak shock, while in flight the undissociated gas is processed by a strong shock. Depending on the conditions, the result of the relaxation processes may be similar. In fact, if the combination of pressure and shock stand-off distance is similar and the relaxation processes are common, then the gas may reach the same thermochemical state as it approaches the surface in both cases. There is much to be done to establish the validity of this hypothesis, but the spatially resolved radial temperature profile measurements in the shock layer represent an important first step in this process. These measurements showed agreement between the three temperatures; T_r, T_v, and T_e; over a fairly large shock layer region at the low pressure, low current condition. This suggests that the gas is in thermal equilibrium at a lower shock layer pressure than was expected. As mentioned above, further work to assess the chemical state of the gas in this region of the shock layer is ongoing, and some of this effort is directed toward relating the conditions of this test to the appropriate flight environment. Finding a region of thermal equilibrium, and possibly chemical equilibrium, within the shock layer provides a foundation for further characterization of the shock layer flow, and, more importantly, a basis for interpreting test results without having to make assumptions about the state of the test gas reaching the surface.

These admittedly intermediary and preliminary findings have not yet made a convincing case for the use of arcjets as aerothermodynamic ground test facilities. It also appears likely that the possibility of performing aerothermodynamic tests in arcjet facilities will depend on the operating conditions and the test configuration. However, the results acquired from the optical diagnostic measurements in a prototypical large-scale arcjet test facility argue strongly for further careful measurements to continue toward this goal.

5. Acknowledgements

A number of talented and dedicated researchers have contributed to this work, and their efforts are greatly appreciated. Special thanks are owed to Chung Sik Park, James Donohue, Mark Newfield, Tahir Gökçen, Imelda Terazzas-Salinas, John Balboni, Chul Park, Doug Bamford, Jochen Marschall, George Raiche, and Frank Hui. The support of the Reacting Flow Environments Branch and the Space Technology Division at Ames Research Center are gratefully acknowledged. Finally, the efforts of the technical staff of the Thermophysics Facilities Branch ensured reliable and repeatable arcjet facility performance, without which this work would not have been possible.

6. References

1. A. Balter-Peterson, F. Nichols, B. Mifsud, and W. Love, "Arc Jet Testing in NASA Ames Research Center Thermophysics Facilities", AIAA Paper No. 92-5041, th *AIAA International Aerospace Planes Conference*, (American Institute of Aeronautics and Astronautics, New York, 1992).
2. C. Scott, "Survey of Measurements of Flow Properties in Arcjets",*Journal of Thermophysics and Heat Transfer*,**7**, pp. 9-24, (1993).
3. A. Okuno and C. Park, "Stagnation Point Heat Transfer Rate in Nitrogen Plasma Flows: Theory

and Experiment", *Journal of Heat Transfer*, pp. 372-384, August, (1970).

4. R. L. McKenzie, "Progress in Laser Spectroscopic Techniques for Aerodynamic Measurements: An Overview", *AIAA J.*, **31**, pp. 465-477, (1993).
5. A. C. Eckbreth, Laser Diagnostics for Combustion Temperature and Species, Abacus Press, Tunbridge Wells, (1988).
6. W. Demtröder, Laser Spectroscopy, 2^{nd} Ed., Springer-Verlag, Berlin, (1996).
7. G. Herzberg, Molecular Spectra and Structure, Vol. I - Spectra of Diatomic Molecules, 2^{nd} Edition, Krieger Publishing Company, Malabar, (1989).
8. K. P. Huber and G. Herzberg, Constants of Diatomic Molecules, Van Nostrand Reinhold, New York, (1979)
9. C. O. Laux, "Optical Diagnostics and Radiative Emission of Air Plasmas", Stanford High Temperature Gasdynamics Laboratory Report No. HTGL T-288, Stanford University, August, (1993).
10. W. G. Vincenti and C. H. Krueger Jr., Introduction to Physical Gas Dynamics, R. E. Krieger, Malabar, 108-109, (1982).
11. ibid, pp. 448-460.
12. T. Gökçen, C. S. Park, M. E. Newfield, and D. G. Fletcher, "Computational Simulation of Emission Spectra from Shock Layer Flows in an Arc-Jet Facility", J. Thermophysics and Heat Transfer **12**, 180-189, (1998).
13. E. E. Whiting, J. O. Arnold, and G. C. Lyle, "A Computer Program for a Line-by-Line Calculation of Spectra from Diatomic Molecules and Atoms Assuming a Voigt Line Profile", NASA TN D-5088, March, (1969).
14. C. S. Park, M. E. Newfield, D. G. Fletcher, T. Gökçen, and Sharma, S. P., "Spectroscopic Emission Measurements within the Blunt Body Shock Layer in an Arc-Jet Flow", AIAA Paper No. 97-0990, Jan., 1997, also *J. Thermophysics and Heat Transfer*, **12**, pp. 190-197, (1998).
15. E. E. Whiting, C. Park, Y. Liu, J. O. Arnold, and J. A. Paterson, "NEQAIR96, Nonequilibrium and Equilibrium Radiative Transport and Spectra Program: User's Manual", NASA Reference Publication 1389, and references therein, (1996).
16. W. L. Wiese, J. R. Fuhr, and T. M. Deters, "Atomic Transition Probabilities of Carbon, Nitrogen, and Oxygen: A Critical Compilation", *J. Phys. Chem. Ref. Data*, Monograph No. 7, (1994).
17. C. Park and D. Moore, "A Polynomial Method for Determining Local Emission Intensity by Abel Inversion", NASA TN D-5677, Feb., (1970).
18. W. E. Bruce and D. D. Horn, "AEDC Arc Column Diagnostic Measurements", ISA Paper No. 92-0190, (1992).
19. J. S. Taunk, C. E. Shepard, and A. Carrasco, "Design and Verification of a Copper Disk for Radiation Measurement in the Constrictor Region of an Arcjet", ISA Paper No. 94-3025, Baltimore, MD, (1994).
20. I. Terrazas-Salinas, C. Park, A. W. Strawa, N. K. J. M. Gopaul, and J. S. Taunk, "Spectral Measurements in the Arc Column of an Arc-Jet Wind Tunnel, AIAA Paper No. 94-2595, (1994).
21. V. R. Watson and E. B. Pegot, "Numerical Calculations for the Characteristics of a Gas Flowing Axially Through a Constricted Arc", NASA TN D-4022, June, (1967).
22. M. A. Rob, L. H. Mack, S. Arepalli, and C. D. Scott, "Spectral Measurements in the Plenum of an Arcjet Wind Tunnel", AIAA Paper No. 95-2126, 30^{th} AIAA Thermophysics Conference, San Diego, CA, (1995).
23. M. A. Rob, L. H. Mack, S. Arepalli, and C. D. Scott, "Characterization of Plenum Spectra in an Arcjet Wind Tunnel", *J. Thermophysics and Heat Transfer*, **11**, pp. 339-345, (1997).
24. L. H. Mack, M. A. Rob, S. Arepalli, C. D. Scott, J. D. Milhoan, and C. O. Laux, "Radial Spectral Measurement in the Plenum of an Arc-Jet Wind Tunnel", AIAA Paper No. 96-1897, (1996).
25. J. M. Donohue, D. G. Fletcher and C. S. Park, "Emission Spectral Measurements in the Plenum of an Arcjet Wind Tunnel", AIAA Paper No. 98-2946, 7^{th} AIAA/ASME Joint Thermophysics and Heat Transfer Conference, June, (1998).
26. N. K. J. M. Gopaul, "Spectral Measurement of Nonequilibrium Arc-Jet Free Stream Flow", ISA Paper No. 93-144, *39^{th} International Instrumentation Symposium*, (International Society for Measurement and Control, Research Triangle Park, 1993).
27. D. S. Babikian, N. K. J. M. Gopaul, C. Park, "Measurement and Analysis of Nitric Oxide Radiation in and Arcjet Flow", *J. Thermophysics and Heat Transfer*, **8**, pp. 737-743, (1994).
28. C. S. Park, M. E. Newfield, D. G. Fletcher, and T. Gökçen "Spectroscopic Measurements of the Flows in an Arc-Jet Facility", AIAA Paper No. 98-0893, *36^{th} Aerospace Sciences Meeting*, (American Institute of Aeronautics and Astronautics, New York, 1998),also *J. Thermophysics and Heat Transfer*, **13**, pp.60-67, (1999).
29. C. S. Park, D. G. Fletcher, and J. M. Donohue, "Spatially Resolved Shock Layer Emission Measurements and Analysis in an Arc-Jet Facility", AIAA Paper No. 99-1046, *37^{th} Aerospace Sciences Meeting*, (American Institute of Aeronautics and Astronautics, New York, 1999).
30. H. E. Blackwell, F. A. Wierum, and C. D. Scott, " Spectral Determination of Nitrogen Vibrational Temperatures", AIAA Paper No. 87-1532, AIAA 22^{nd} Thermophysics Conference, June, (1987).
31. H. E. Blackwell, F. A. Wierum, S. Arepalli, and

C. D. Scott, "Vibrational Measurements of N_2 and N_2^+ Shock Layer Radiation", AIAA Paper No. 89-0248, AIAA 27^{th} Aerospace Sciences Mtg., January, (1989).

32. G. A. Raiche, "Molecular Ultraviolet and Visible Emission from an Air Arc Jet Bow Shock", ISA Paper No. 94-3020, *40^{th} International Instrumentation Symposium*, (International Society for Measurement and Control, Research Triangle Park, 1994).
33. D. S. Babikian, C. Park, and G. A. Raiche, "Spectroscopic Determination of Enthalpy in an Arc-Jet Wind Tunnel", AIAA Paper No. 95-0712, *33^{rd} Aerospace Sciences Meeting*, (American Institute of Aeronautics and Astronautics, New York, 1995).
34. H. E. Blackwell, C. D. Scott, and S. Arepalli, "Measured Nonequilibrium Temperatures in a Blunt Body Shock Layer in Arc Jet Nitrogen Flow", AIAA Paper No. 97-2522, AIAA 32^{nd} Thermophysics Conference, June, (1997).
35. M. W. Winter, M. Auweter-Kurtz, H. L. Kurtz, and C. Park, "Investigation of an Equilibrium Condition Boundary Layer in Front of a Material Probe in a Subsonic Plasma Flow", AIAA Paper No. 96-1853, 31^{st} AIAA Thermophysics Conference, June, (1996).
36. M. W. Winter, M. Auweter-Kurtz, and H. L. Kurtz, "Spectroscopic Investigation of the Boundary Layer in Front of a Blunt Body in a Subsonic Air Plasma Flow", AIAA Paper No. 97-2526, AIAA 32^{nd} Thermophysics Conference, June, (1997).
37. A. C. Eckbreth, Laser Diagnostics for Combustion Temperature and Species, pp. 304-310, Abacus Press, Tunbridge Wells, (1988).
38. R. C. Hilborn, "Einstein Coefficients, Cross Sections, *f* Values, Dipole Moments, and All That", *American Journal of Physics*, **50**(11), pp. 982-986, November, (1982).
39. S. Arepalli, E. H. Yuen, and C. D. Scott, "Application of Laser-Induced Fluorescence for Flow Diagnostics in Arc Jets", AIAA Paper No. 90-1763, AIAA/ASME 5^{th} Joint Thermophysics Conference, Seattle, WA, June, (1990).
40. W. J. Marinelli, W. J. Kessler, M. G. Allen, and S. J. Davis, "Copper Atom Based Measurements of Velocity and Turbulence in Arc Jet Flows", AIAA paper No. 91-0358, AIAA 29^{th} Aerospace Sciences Meeting, Reno, NV, (1991).
41. K. Itagaki, T. Yamada, Y. Inatani, and K. Suzuki, "Measurement of Two-Dimensional Velocity Distribution of Arc-Heated Flow by Cu-LIF", Paper No. 96-d-19, 20^{th} International Symposium on Space Technology and Science, Gifu, Japan, May, (1996).
42. T. Takahashi, T. Yamada, and Y. Inatani, "Measurement of NO Rotational and Vibrational Temperatures in Arc Heated Air Flow by LIF Spectroscopy", Paper No. 96-d-18, 20^{th} International Symposium on Space Technology and Science, Gifu, Japan, May, (1996).
43. M. Feigl and M. Auweter-Kurtz, "Investigation of Nitric Oxide in a High Enthalpy Air Plasma Flow Using Laser-Induced Fluorescence", AIAA Paper No. 98-2459, 7^{th} AIAA/ASME Joint Thermophysics Conference, Alburquerque, NM, June, (1998).
44. D. J. Bamford, "Remote Measurement System for Arcjet Temperature and Density", Deacon Research Phase II SBIR Final Report, Contract No. NAS2-13469, (1993).
45. W. K. Bischel, B. E. Perry, and D. R. Crosley, "Detection of Fluorescence from O and N Atoms Induced by Two-Photon Absorption", *Applied Optics*, **21** (8), pp. 1419-1429, April, (1982).
46. D. J. Bamford, A. O'Keefe, D. S. Babikian, D. A. Stewart, and A. W. Strawa, "Characterization of Arc-Jet Flows Using Laser-Induced Fluorescence", J. Thermophysics and Heat Transfer **9**, 26-33, (1995).
47. D. J. Bamford and A. Romanovsky, "Velocity and Chemical Composition Measurements in an Arc Jet Flow", AIAA Paper No. 95-2039, *30^{th} AIAA Thermophysics Conference*, (American Institute of Aeronautics and Astronautics, New York, 1995).
48. D. G. Fletcher, "Arcjet Flow Properties Determined from Laser-Induced Fluorescence of Atomic Nitrogen", AIAA Paper No. 98-0205, *36^{th} Aerospace Sciences Meeting*, (American Institute of Aeronautics and Astronautics, New York, 1998).
49. D. G. Fletcher and D. J. Bamford, "Arcjet Flow Characterization Using Laser-Induced Fluorescence of Atomic Species", AIAA Paper No. 98-2458, *7^{th} AIAA/ASME Joint Thermophysics and Heat Transfer Conference*, (American Institute of Aeronautics and Astronautics, New York, 1998).
50. D. J. Bamford, L. E. Jusinski, and W. K. Bischel, "Absolute two-photon absorption and three-photon ionization cross sections for atomic oxygen", Phys. Rev. A **34**, 185-198, (1986).
51. R. Loudon, The Quantum Theory of Light, 2^{nd} Ed., Clarendon Press, Oxford, pp. 344-347, (1986).
52. D. G. Fletcher and J. C. McDaniel, "Collisional Shift and Broadening of I_2 Spectral Lines in Air Near 543 nm", JQSRT **54**, 837-850, (1995).
53. J. B. Jeffries, R. A. Copeland, and D. R. Crosley, "Intramultiplet energy transfer in the collisions of $3p^4D^\circ$ nitrogen atoms with nitrogen molecules", J. Chem. Phys. **91**, 2200 - 2205, (1989).
54. W. K. Bischel, D. J. Bamford, and L. E. Jusinski, "Absolute calibration of a fluorescence collection system by Raman scattering of H_2", Appl. Opt. **25**, 1215-1221, (1986).
55. R. A. Copeland, J. B. Jeffries, A. P. Hickman, and D. R. Crosley, "Radiative lifetime and quenching of the $3p^4D^\circ$ state of atomic nitrogen", J. Chem.

Phys. **86**, 4876-4884, (1987).

56. J. Balboni, Thermophysics Facilities Branch, NASA Ames Research Center, private communication, August, 1997.
57. H. W. Leipmann and A. Roshko, Elements of Gasdynamics, John Wiley & Sons, New York, 149, (1957).
58. W. G. Vincenti and C. H. Krueger Jr., Introduction to Physical Gas Dynamics, R. E. Krieger, Malabar, 152-158, (1982).
59. I. J. Wysong, J. B. Jeffries, and D. R. Crosley, "Laser-Induced Fluorescence of O(3p ^{3}P), O_2, and NO Near 226 nm: Photolytic Interferences and Simultaneous Excitation in Flames", *Optics Letters*, **14**, pp. 767-769, (1989).